

Fracture aperture generation using surface scan measurements of natural rock samples

Brandon Stock¹ and Andrew Frampton¹

¹Stockholm University

September 25, 2023

Abstract

In sparsely fractured crystalline rock, aperture variability exhibits significant control of the flow field through the fracture network. However, its inclusion in models is hampered due to a lack of field measurements and adequate numerical representation. A model for aperture generation is developed based on self-affine methods which includes two key parameters, the Hurst exponent and a scaling parameter, and which accounts for relative anisotropy and correlation between the adjacent surfaces forming the fracture. A methodology for analysing and extracting the necessary parameters from 3D surface scans of natural rock fractures is also developed. Analysis of the Hurst exponent and scaling parameter space shows that input combinations following a linear upper bound can be used to generate aperture fields which accurately reproduce measurements. It is also shown that the Hurst and scaling parameters are more sensitive than the correlation between the upper and lower fracture surfaces. The new model can produce an aperture ensemble that closely corresponds with the aperture obtained from the surface scans, and is an improvement on previous methods. The model is also successfully used to up-scale fracture apertures based on measurements restricted to a small sub-section of the sample. Thereby, the aperture fields generated using the model are representative of natural fracture apertures and can be implemented in larger scale fracture network models, allowing for numerical simulations to include representation of aperture internal heterogeneity.

1 **Fracture aperture generation using surface scan**
2 **measurements of natural rock samples**

3 **Brandon Stock¹, Andrew Frampton^{1,2}**

4 ¹Department of Physical Geography, Stockholm University, Stockholm, Sweden

5 ²Bolin Center for Climate Research, Stockholm University, Stockholm, Sweden

6 **Key Points:**

- 7 • A model for aperture generation based on self-affine theory is improved and eval-
8 uated using surface scans of a natural rock sample
- 9 • A linear correlation between Hurst exponent and scaling parameter can accurately
10 reproduce the aperture distribution of the natural fracture
- 11 • The improved model is shown to successfully generate up-scaled aperture fields
12 using subsections of the natural rock surface

Corresponding author: Brandon Stock, Brandon.Stock@natgeo.su.se

Abstract

In sparsely fractured crystalline rock, aperture variability exhibits significant control of the flow field through the fracture network. However, its inclusion in models is hampered due to a lack of field measurements and adequate numerical representation. A model for aperture generation is developed based on self-affine methods which includes two key parameters, the Hurst exponent and a scaling parameter, and which accounts for relative anisotropy and correlation between the adjacent surfaces forming the fracture. A methodology for analysing and extracting the necessary parameters from 3D surface scans of natural rock fractures is also developed. Analysis of the Hurst exponent and scaling parameter space shows that input combinations following a linear upper bound can be used to generate aperture fields which accurately reproduce measurements. It is also shown that the Hurst and scaling parameters are more sensitive than the correlation between the upper and lower fracture surfaces. The new model can produce an aperture ensemble that closely corresponds with the aperture obtained from the surface scans, and is an improvement on previous methods. The model is also successfully used to up-scale fracture apertures based on measurements restricted to a small sub-section of the sample. Thereby, the aperture fields generated using the model are representative of natural fracture apertures and can be implemented in larger scale fracture network models, allowing for numerical simulations to include representation of aperture internal heterogeneity.

Plain Language Summary

Understanding fluid flow through naturally fractured rock is important for several applications, including subsurface infrastructure and storage of nuclear waste. Many studies assume fractures as smooth planes; however, it is known that real fractures have rough surfaces and a variable aperture, and this variability can significantly control water flow. It is difficult to include an accurate representation of aperture variability in models because of a lack of field measurements, as well as difficulties in creating adequate model-based representations of the variable aperture field. In this study, improvements are made to a previously developed approach for aperture generation, which is based on self-affine theory. The theory is founded on observations of fractal behaviour exhibited by rock surfaces. It is shown that parameter combinations that follow a linear upper bound can be used to generate aperture fields that accurately reproduce the measured apertures. The model is also successfully used to generate up-scaled aperture fields based on a subsection of the fracture sample. Aperture fields generated using this model are representative of natural fracture apertures and can be used in larger scale models, allowing for a realistic representation of aperture variability to be included when simulating flow in models for fractured rock.

1 Introduction

Understanding fluid flow through natural fractured rocks systems is important for several applications, including subsurface infrastructure, storage facilities for spent nuclear fuel and other toxic waste, and hydrocarbon industries (Tsang & Neretnieks, 1998). Flow and transport through sparsely fractured rock is often modelled using a discrete fracture network (DFN) approach because it is well-suited to numerically represent the typically complex geometries observed in fractured bedrock (Cacas et al., 1990; Framp-ton & Cvetkovic, 2011; Lang et al., 2014). Representation of fractures in DFN models is typically based on the parallel-plate assumption (Witherspoon et al., 1980; Zimmerman & Bodvarsson, 1996), where fracture permeability is often used to represent the aperture void space within fractures. However, DFN models often simplify the effect of internal aperture variability by assuming constant or effectively homogeneous hydraulic properties within the plane of individual fractures. Although most DFN models are able

63 to numerically include internal variability, its representation is hampered by a lack of
64 field measurements. Also, homogenisation allows for a computationally less demanding
65 description of the fluid flow between fractures, which simplifies run times for large DFNs.
66 Nonetheless, it is well known that fractures are rough walled conduits with varying aper-
67 ture and multiple contact points (Durham & Bonner, 1994; Novakowski & Lapcevic, 1994;
68 Hakami, 1995; S. R. Brown, 1998), and studies have shown that these features can ex-
69 hibit control of the flow field through both single fractures (S. Brown, 1987; Nicholl et
70 al., 1999; Zou et al., 2017) as well as fracture networks (Frampton et al., 2019).

71 Fracture surface roughness has been shown to exhibit self-affine fractal properties
72 (S. Brown, 1987; Power & Tullis, 1991; Renard et al., 2006). Self-affine differ from self-
73 similar fractals as they scale anisotropically along horizontal and vertical reference axes
74 whereas self-similar scale isotropically (Mandelbrot, 1982; Power & Tullis, 1991). The
75 fractal dimension, D , of the surface describes the complexity of the fractal (Malinverno,
76 1990; Power & Tullis, 1991), and the Hurst exponent, $H = E - D$ (Hurst, 1951), is a mea-
77 sure of the randomness, where E is the number of spatial dimensions in which the frac-
78 tal is measured. The values of D for rock fractures typically range from 1-1.5 for pro-
79 files and 2-2.5 for surfaces (S. Brown, 1987). This agrees with the definition of self-affine
80 fractals where $D = 1.5$ for profiles compared to self-similar definition where $D = 2$ (S. Brown,
81 1987). When describing fracture surfaces using fractals, the Hurst exponent is more con-
82 venient (Gallant et al., 1994).

83 Therefore, in order to generate fractures with internal variability, for example for
84 use in numerical DFN models for flow and transport, the methods used should preserve
85 the self-affine properties of the natural rough-surfaced fractures they aim to reproduce.
86 This includes the Hurst exponent and scaling parameter, but also surface height vari-
87 ability, relative anisotropy, and correlation between the upper and lower surfaces form-
88 ing the fracture aperture (Ogilvie et al., 2006). Another aspect to take into considera-
89 tion is the stochastic nature of aperture generation and its needs for numerical DFN mod-
90 elling. Typically, a large number of fractures are used in models, far more than can re-
91 alistically be sampled and studied from field investigation. Therefore it is desirable to
92 be able to generate multiple fractures based off of a limited set of fracture aperture mea-
93 surements, thereby using the same or small set of input parameters to generate multi-
94 ple fracture realisations (Isakov et al., 2001; Ogilvie et al., 2003). Furthermore, DFN mod-
95 els typically require fractures to be generated at multiple spatial scales, and often at a
96 much greater scale than available from measurements. Thus there is a practical need to
97 upscale fractures, and here, self-affine methods are well suited as spatial rescaling is in-
98 herent to their design.

99 Natural fractures are complex to replicate due to their anisotropy and the corre-
100 lation exhibited between the upper and lower rough surfaces forming the aperture void
101 space. A root-mean squared (RMS) correlation function has successfully been used to
102 characterise anisotropy on exposed structures (Candela et al., 2009). To obtain variable
103 aperture, two partially correlated rough surfaces are needed. Although generation of in-
104 dependent surfaces is relatively easy, correlation and separation between two surfaces is
105 needed for creating realistic fracture apertures. It is understood that correlation between
106 the surfaces is weak at short wavelengths, where the surface variabilities act reasonably
107 independently of each other, but becomes stronger, and reaches a peak, as wavelength
108 increases (S. Brown, 1987; S. R. Brown & Scholz, 1985; Keller et al., 1999; Ogilvie et al.,
109 2006). Surfaces have been found to be well correlated above the scale of a few millime-
110 tres (S. R. Brown & Scholz, 1985; Power & Tullis, 1992).

111 Several attempts have been made to represent the change in correlation with scale.
112 Previous work by S. R. Brown (1995b) proposed a second surface generated with a ‘mis-
113 match length scale’. The wavelengths for the mismatch were obtained from the power
114 spectral density ratio (PSDR). The surfaces are well-correlated at large wavelengths and
115 uncorrelated when the wavelength becomes less than the assigned mismatch length scale.

116 A set of random numbers can be used to define the phase of the Fourier components which
117 are used to generate the upper and lower surfaces. The correlation between the random
118 number set at different length scales therefore determines the correlation between sur-
119 faces of the generated aperture. S. R. Brown (1995b) implemented the uncorrelated length
120 scale by using a second random number generator different from the one used to pro-
121 duce the first surface. This decorrelates the surfaces at scales below the mismatch length,
122 and amplitudes for wavelengths greater than the mismatch length use the same num-
123 ber generator as the one used to create the first surface. This creates a sharp disconti-
124 nuity between correlated and uncorrelated surfaces. However, Glover et al. (1998b) ar-
125 gued that the transition should be smooth, following a frequency dependent change from
126 high to low correlation. The PSDR function of the surfaces combined with a weighting
127 function was suggested which determines the rate at which the surfaces match with re-
128 spect to frequency.

129 Glover et al. (1998b) required two independent random number sets for the wave-
130 lengths that are less than the mismatch wavelength, and above this the random num-
131 bers are partially correlated. This involved mixing sets of two random numbers using
132 linear weighting. However, Ogilvie et al. (2006) noted that algebraically mixing random
133 number sets in this manner breaks down the distribution produced by the random num-
134 ber generator. Therefore, they proposed an algorithm which swaps the positions of num-
135 bers in two random number sets until the desired correlation is reached, producing a par-
136 tially correlated random number data set. This has the advantage of maintaining the
137 distribution produced by the random number generator as well as enabling the corre-
138 lation to vary with scale between the two surfaces, producing a more accurate aperture.

139 Ogilvie et al. (2006) uses several parameters to determine how the matching be-
140 tween surfaces changes with scale based on the PSDR. These are an improvement on pre-
141 vious methods as a minimum and maximum matching fraction can be set and how the
142 change in correlation varies between these two points. However, the overall change from
143 low to high correlation is still a linear change, and even with added parameters to in-
144 crease the accuracy, it still may not represent natural fractures. That study was also per-
145 formed on synthetically induced mode I fractures; thus, it is not yet known how well these
146 methods perform when using measurements from and comparing against real-world nat-
147 ural rock fractures.

148 The aim of this study is to develop and evaluate a method for reproducing rough-
149 surfaced fractures with variable aperture using information obtained from 3D scans of
150 natural rock fracture surfaces. A model for stochastic fracture aperture generation is fur-
151 ther developed based on previous work using self-affine fractal concepts, which includes
152 a refined method for representing correlation between the upper and lower surfaces of
153 the fracture. The model is used to generate an ensemble of realisations of fracture aper-
154 tures, which is evaluated against the measured natural fracture aperture. Furthermore,
155 a detailed sensitivity analysis is conducted on the variability of the Hurst and scaling
156 parameters and the correlation obtained from the surface scans of the fracture in terms
157 of their impact on model performance. Finally, the model is evaluated in terms of spa-
158 tial up-scaling, where a subsection of the measurements are used to predict the full ex-
159 tent of the fracture.

160 2 Method

161 A spectral synthesis approach is used to numerically produce fractals that repre-
162 sent two surfaces which when combined form a fracture with variable aperture void space.
163 A symmetric matrix containing Fourier components is defined, where the Fourier com-
164 ponents can be obtained from measurements to obey the various desired properties of
165 the fracture. Each component is comprised of an amplitude and a phase. Fractal dimen-
166 sion and any information about relative anisotropy is contained within the amplitude

167 component that scales with a power law. Thus, the topography of the fracture surfaces
 168 are controlled by the phase of the Fourier components. If the phase is identical for the
 169 upper and lower surfaces, the resulting fracture aperture is constant, representing a per-
 170 fectly mated fracture. In order to create a variable aperture field, the topography of the
 171 two surfaces need to be uncorrelated or partially correlated at different wavelengths. When
 172 random numbers are used to describe the phase of the Fourier components, the degree
 173 of matedness between the surfaces can be controlled by the degree of correlation between
 174 the random numbers used.

175 Natural rock surfaces can be described by a power spectral density function (S. R. Brown,
 176 1995a),

$$177 \quad G(k) = Ck^{-\alpha} \quad (1)$$

178 where $k = 2\pi/\lambda$ is the wavenumber, λ is the wavelength which corresponds to distance
 179 along the profile, C is a proportionality constant which varies among surfaces and cor-
 180 responds to the intercept of the logarithm of the power spectrum, and α is the fractal
 181 dimension in the range of $2 < \alpha < 3$ which corresponds to the slope of the logarithm of
 182 the power spectrum. To obtain the correlation between the upper and lower surfaces of
 183 the fracture scans, the power spectral density (PSD) of each surface and the resulting
 184 aperture needs to be obtained, which can readily be calculated using Fast Fourier Trans-
 185 forms.

186 In principle the Fourier decomposition of a surface can be done for an infinite num-
 187 ber of wavenumbers k , however in practice there is a clear limit. The limit is defined by
 188 the resolution of the surface scans, and any pre-processing interpolation that has been
 189 done before calculating the PSD of the fracture surface. When the period of the sine waves
 190 are equal to the number of mesh cells in one dimension, then each oscillation of the sine
 191 wave exactly covers one cell. Increasing the resolution beyond this point so more sine
 192 waves cover a single cell would have no further effect on the amplitude. The maximum
 193 frequency that is useful for the surface is therefore $k = 1/N$, where N is the maximum
 194 number of cells along one edge length of the fracture scan. When $k = 1$ this corresponds
 195 to a sine wave that fits exactly once within the surface.

196 2.1 Correlation analysis

197 The correlation of the upper and lower fracture surfaces can be calculated by us-
 198 ing the ratio of the PSD from the aperture over the sum of the PSDs of the two surfaces;
 199 it is convenient to plot it as a function of wavelength on log-log scale. Ogilvie et al. (2006)
 200 called this the PSD Ratio (PSDR, $\xi(k)$), where

$$201 \quad \xi(k) = \frac{G(k)_{\text{aperture}}}{G(k)_{\text{upper surface}} + G(k)_{\text{lower surface}}} \quad (2)$$

202 If the PSD ratio tends towards unity for all wavenumbers then the surfaces are completely
 203 independent (Glover et al., 1998b, 1998a). If the PSDR is less than unity, then some match-
 204 ing correlation is occurring between the upper and lower fracture surfaces at that spe-
 205 cific wavenumber. The correlation at each wavenumber is obtained as $\text{Corr}(k) = 1 -$
 206 $\xi(k)$. Here we introduce a polynomial regression over the PSDR obtained from measure-
 207 ments of a rock fracture from the smallest to largest PSDR(k) value as a convenient ap-
 208 proach to remove the fluctuations and get values for the general trend as a function of
 209 wavenumber (or wavelength). Fluctuations in the PSDR inevitably occur when calcu-
 210 lating the PSD from measurements of fracture surfaces due to natural variability in the
 211 upper and lower surface as well as measurement precision.

212 During aperture generation, different quantities of wavenumbers may be required,
 213 and will not necessarily match the amount coming from the measurements of a real frac-
 214 ture. Therefore, the correlation values are typically re-scaled along the length direction
 215 of a profile to the correct number of values that are needed for the generation method.

216 Due to the method of generating a self-affine fractal surface, the dimensions are limited
 217 to $2 \times 2^n + 1$ in X and Y , so the correlation values are scaled in length to 2^n , which is
 218 half of the desired edge length of which the aperture will be generated at. This is im-
 219 portant as it will maintain the desired correlation and structure regardless of the reso-
 220 lution used to generate the aperture.

221 Fractures typically have high correlation at small wavenumbers (large wavelengths),
 222 indicating there is large-scale correlation across the fracture. As the wavenumber increases
 223 (and wavelength decreases) the matching between the surfaces typically decreases. Once
 224 the correlation function $\text{Corr}(k)$ is obtained, a number swapping algorithm is used to cre-
 225 ate several arrays of different correlation which represent the different wavenumbers. We
 226 adopted a method similar to Ogilvie et al. (2006), and developed a number swapping al-
 227 gorithm that swaps the positions of numbers within one random normally distributed
 228 array until a set correlation, defined by the matching analysis, is reached between the
 229 other random normally distributed array. The algorithm is executed several times such
 230 that two correlated arrays are created for every wavenumber that is needed. Correlated
 231 pairs of values are selected from the arrays and are placed in two grids that represent
 232 the upper and lower surface in the corrected position depending on the wavenumber. This
 233 creates a partial correlation between the upper and lower surface that changes with scale.
 234 To create different realisations different pairs are randomly selected from the arrays, and
 235 the phase of the Fourier components is defined by these random number sets.

236 2.2 Scaling properties

237 The other properties needed to generate a self-affine fractal surface are the Hurst
 238 exponent H and a scaling parameter. For a self-affine profile to appear similar at dif-
 239 ferent scales, it must be scaled anisotropically in two different directions, i.e., length ver-
 240 sus topographical height of a rough surface. If the abscissa (length) is scaled by a fac-
 241 tor of λ , the ordinate (height) needs to be scaled by λ^H . We adopt the RMS-COR method
 242 (Malinverno, 1990; Renard et al., 2006; Candela et al., 2009; Stigsson & Mas Ivars, 2019)
 243 to analyse the standard deviation of height difference at different length intervals; at ver-
 244 tices Δv apart the standard deviation σ of the height differences δh is obtained as:

$$245 \quad \sigma(\delta h(\Delta v)) = \sqrt{\frac{\sum_{v=0}^{N-\Delta v} (h(v + \Delta v) - h(v))^2}{N + 1 - \Delta v} - \left(\frac{\sum_{v=0}^{N-\Delta v} (h(v + \Delta v) - h(v))}{N + 1 - \Delta v} \right)^2} \quad (3)$$

246 where Δv is the number of vertices between the height values being analysed, $h(v)$ is the
 247 height value at vertex v , and N is the number of vertices within the line. The Hurst ex-
 248 ponent H is obtained by a log-log fit of the standard deviations σ against the distance
 249 between the vertices Δv ; the slope of the line corresponds to H and the intercept cor-
 250 responds to the standard deviation of adjacent vertices δh , the value which is used to
 251 scale generated surfaces.

252 The method is relatively easy to implement but affected by the finite length of trace
 253 profiles. Therefore, Δv must be small compared to N ; for this reason if Δv is above ap-
 254 proximately 10% of maximum trace length it is not considered reliable (Marsch & Fernandez-
 255 Steeger, 2021). The Hurst exponent can also be underestimated due to the finite trace
 256 length. However, the RMS-COR method is considered to under-estimate Hurst expo-
 257 nents when $H > 0.5$ (Stigsson & Mas Ivars, 2019). Therefore, we implement the fol-
 258 lowing correction as suggested by Marsch and Fernandez-Steeger (2021); if $H_{RMS,cal} >$
 259 0.5 then $H_{RMS} = \ln(H_{RMS,cal}) + 1.18$.

2.3 Surface scans of a natural fracture

The rock sample was taken from a medium grained granite block from the Flivik quarry in Oskarshamn municipality, Sweden, and includes a natural vertical fracture running through it. The sample cut from the rock slab was $200 \times 200 \times 250 \text{ mm}^3$ containing the partially mated fracture. A force of approximately 100 Nm was required to break the remaining rock bridges between the surfaces and open the fracture (Bruines, 2022). Figure 1a shows the fracture surface after opening.

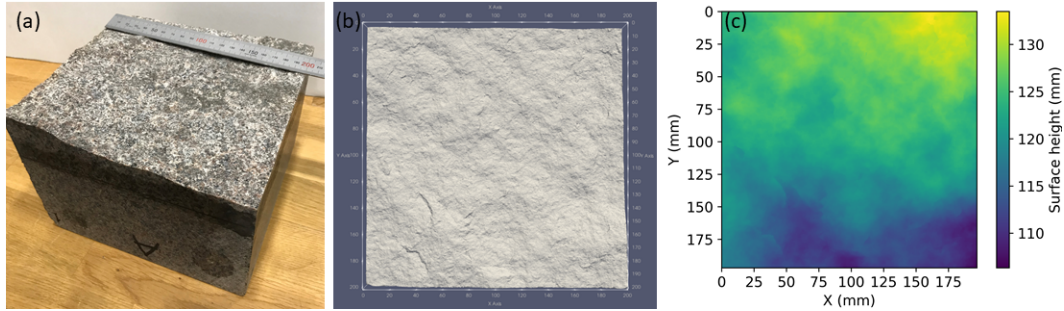


Figure 1. Upper surface of the fracture after opening (a), 3D scan of the surface (b) and surface after interpolation from point cloud data to a regular grid (c).

Once opened, the upper and lower surface were scanned using a handheld laser scanner (Figure 1b). The surface scan data required pre-processing before it could be used to obtain the parameters needed for aperture generation (Stock & Frampton, 2022). The scanning method used results in an irregular mesh. This means on the XY coordinate plane, the nodes on the upper and lower surface will not align. Due to this, the surface data is linearly interpolated onto a regular grid with a resolution of 0.1 mm in order to easily obtain the aperture field (Figure 1c). Areas near the edge of the scan tend to contain errors so the edges are cropped to remove obviously erroneous data. Issues arise from vertical referencing of the upper and lower surface scans, resulting in an unrealistic aperture field with many negative aperture values. To correct this the lower surface is translated relative to the upper surface to improve alignment and reduce inaccurate negative apertures. However, this is insufficient to fully correct the aperture field, so pressure film data that was also provided was used as a reference to vertically shift the upper surface until a visual best fit aperture field distribution is achieved. Further details on pre-processing the surface scan data are presented by Stock and Frampton (2022).

After pre-processing, the surface scans produce an aperture that contains a few abnormal isolated larger apertures, which are most likely due to rock fall out during opening of the fracture. Figure 2 shows the rock fall out collected after opening (a) and the aperture when 5% of the largest apertures have been removed (b). As can be seen, the largest values generally occur in isolated locations across the aperture field. Areas that have a constant value of zero are considered contact points, and areas that are white are where data has been removed (b). An interpretation of the pressure film is also shown (c) with locations of the rock fall out highlighted, white areas represent void spaces that are larger than the thickness of the pressure film ($200 \mu\text{m}$) and red represents a pressure of 50 MPa.

Figure 3 shows the normalised cumulative distribution and box plots for the same aperture whilst systematically filtering the largest values from the data by area. Zero percent represents the full aperture with no data removed and 5% represents the aperture where the largest 5% of aperture values are removed. During opening the fracture, release of stress could lead to the surface level increasing, which results in a negative aper-

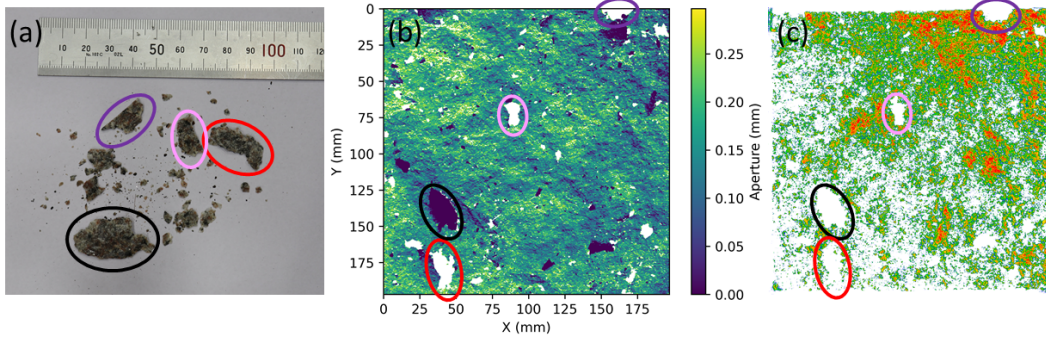


Figure 2. Rock fall out collected after opening the fracture (a) with the possible locations of fall out located on the aperture field by red, black and pink circles (b) and pressure film data (c)

297 ture when the lower surface is subtracted from the upper surface. Therefore, all nega-
 298 tive apertures have been set as zero and are assumed to be contact areas. Removing the
 299 largest 1% of apertures significantly reduces the maximum aperture by approximately
 300 2 mm, this highlights how isolated the largest apertures are. As increasingly larger per-
 301 centages of the aperture are removed, the maximum values decrease whilst only having
 302 small changes on the aperture distribution. The change in distribution is mainly observed
 303 as the normalised cumulative distribution reaches approximately 0.9, and apertures with
 304 a higher percentage of filtering reach the peak sooner. The differences between succes-
 305 sive percentage increase of filtering become smaller, with 4% and 5% having only minor
 306 differences in distribution. Box plots for the distributions (Figure 3b) show a decrease
 307 in most values as larger percentages of the aperture are removed. However, the median
 308 value remains fairly constant, decreasing from 0.149 mm at 0% to 0.146 mm at 5% fil-
 309 tering. The consistency in the medians shows that when the whole aperture is consid-
 310 ered the largest apertures are outliers within the data set. No outliers are present at 5%
 311 filtered, so this aperture is used for comparison with the generated aperture.

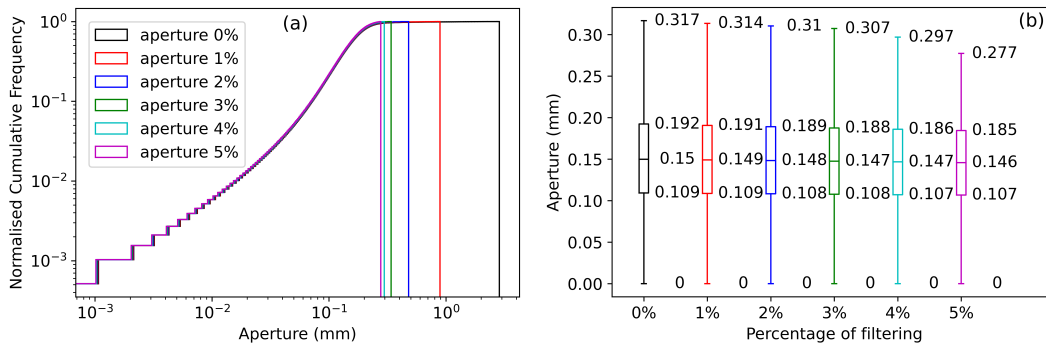


Figure 3. Normalised cumulative distributions of the measured aperture with the maximum apertures filtered by increasing percentages of area (a) and corresponding box plots (b)

312 2.4 Fracture surface and aperture generation

313 Several trace profiles are taken across each of the two fracture surfaces (cf. upper,
 314 shown in Figure 1c) in the X and Y directions along every mesh cell, so that the total
 315 number of profiles in one direction is the same as the total number of cells along one edge

length. This results in 1970 trace profiles in each direction, with a length resolution of each trace profile of 0.1 mm. The RMS-COR method is then executed on every profile, providing a Hurst and scaling parameter for each profile, where a combination of parameters that most closely represents the surface must be selected (section 3.1). Relative anisotropy is calculated by using the median of the ratios $H(X)/H(Y)$. The Hurst exponent and anisotropy are then used to define the amplitude of the Fourier components.

When all the Fourier components are known and arranged in a 2D complex and symmetric matrix in the correct position regarding wavenumber, a 2D Fast Fourier Transformation is executed over the data, the real part of which represents the fracture surface with a mean value of zero. The last steps are to scale the surface to the required size, and scale the asperities to that defined by the scaling parameter obtained from the RMS-COR method, and vertically shift the mean level of the fracture surface such that no negative values occur in the aperture field. It is important to account for different trace resolution between the real data and generated aperture, so the scaling value can be corrected to represent the same resolution, and hence produce an accurate re-scaling of the surface and aperture. Note that the topography of each pair of surfaces will depend on the random number sequence used to select the correlation arrays. Therefore, due to this stochastic nature of sampling, an ensemble of fracture aperture realisations must be generated for a given set of input parameters in order to obtain a sufficiently large sample size to compare against the measured fracture aperture. However, we stress that each generated sample is an equally probably realisation based on a given set of input values. Therefore, this can enable a convenient approach for generating multiple fractures based on a limited number of fracture measurements. Furthermore, since the scaling behaviour of the surface and relative positions of different size asperities is controlled by the Hurst exponent, it enables a convenient approach to up-scaling fracture surfaces, based on the assumption of the properties of the rough surfaces being self-affine for the spatial scales considered and the correlation between surfaces being scale independent.

3 Results

3.1 Fracture surface and aperture field

The PSDR obtained from the fracture with a third order polynomial regression plotted over the PSDR is shown in Figure 4a. The variation in correlation with wavenumber shows the decrease in correlation (Figure 4b, red line) as wavenumber increases. The number of wavenumbers over which the correlation is applied has been re-scaled to correspond with the dimensions at which the aperture realisations will be generated at. As can be seen, the correlation 1 - PSDR (Figure 4b, blue line) initially decreases before increasing again at approximately 50, however the correlation reaches a minimum value of approximately 0.86. The increase thereafter is an artefact due to the resolution of the surface scans and the resolution at which the surfaces were interpolated on to a regular grid. If one value in the point cloud is interpolated over more than one grid cell then 1 - PSDR will increase. This artifact is removed from the correlation array (red line) by manually setting the minimum value for increasing wavenumbers. This adjusted correlation function is then used in the subsequent number swapping algorithm.

The RMS-COR method is then executed on trace profiles across both surfaces in the X and Y directions every 0.1 mm using a maximum step length of 10% (Δv , Eq 3), resulting in 1,970 values of both Hurst exponent and scaling parameter in each direction on the upper and lower surfaces. The 75th percentile for Hurst exponent and scaling parameter have been used to generate the partially correlated upper and lower surfaces and resulting aperture field that are seen in Figure 5. The cumulative density function of the single realisation of the aperture field is shown in Figure 6a. Thereafter, multiple realisations using the same input parameters are generated; the ensemble of 100 realisations are shown in Figure 6b.

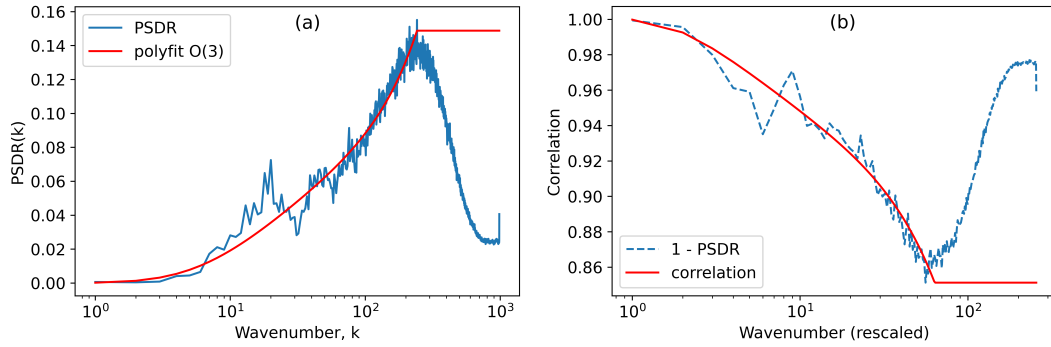


Figure 4. PSDR with a third order polynomial regression (a) and change in correlation with rescaled wavenumbers (b)

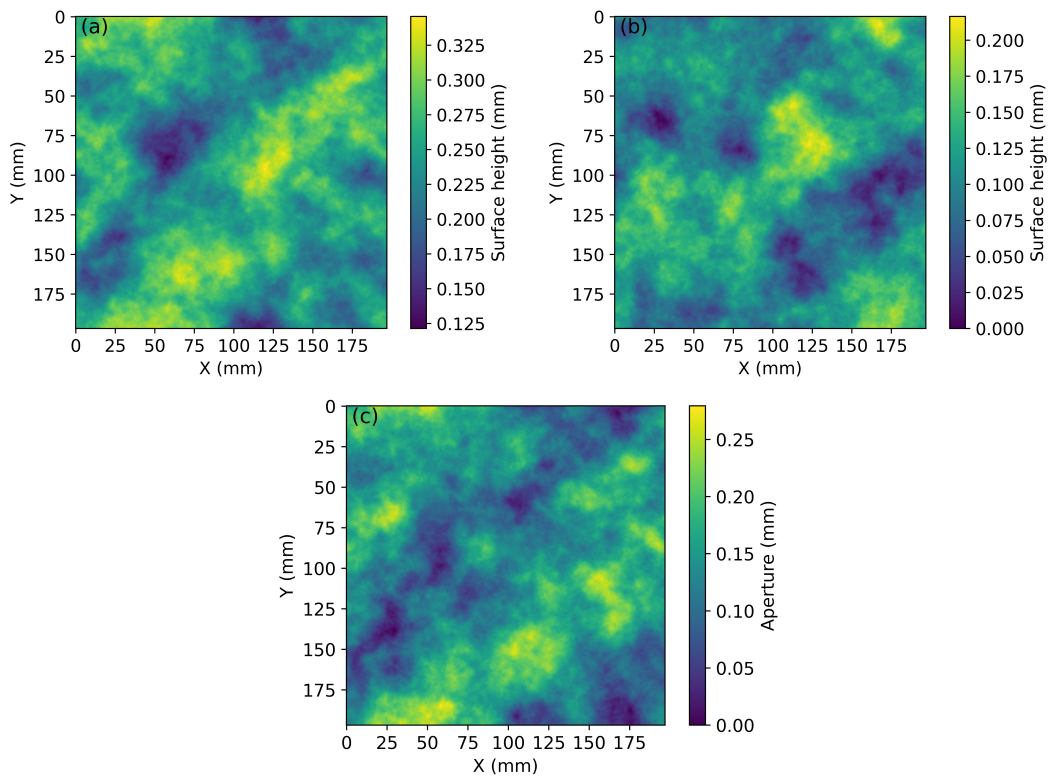


Figure 5. Generated upper surface (a), lower surface (b) and resulting aperture field created from the semi correlated surfaces (c)

367 The spread in aperture distribution is due to the stochastic nature of the method,
 368 therefore multiple realisations are required to be generated until the aperture ensemble
 369 stabilises. The number of realisations required is evaluated by using the two-sided Kolmogorov-
 370 Smirnov test to compare the measured aperture distribution with increasing generated
 371 aperture ensembles (Table 1). A smaller KS value represents a closer match, and a value
 372 of 0 indicates the two empirical distributions are identical. This shows that 50 realisa-
 373 tions and greater will show very little variation; in the main analysis 100 realisations are
 374 used.

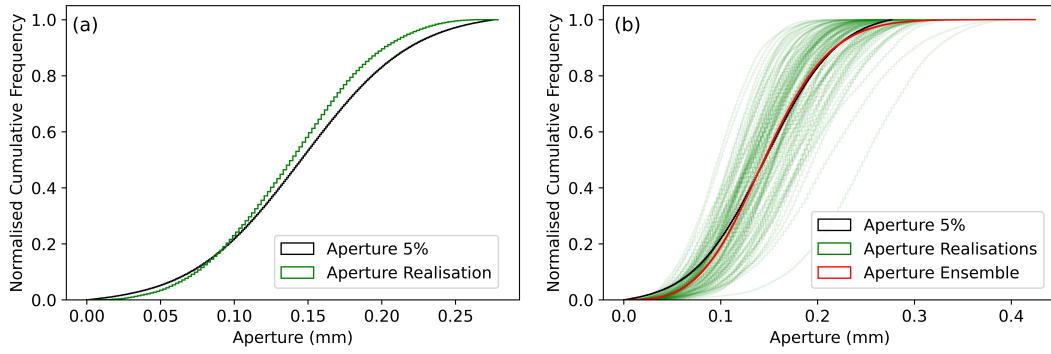


Figure 6. Cumulative distribution of one realisation (a) and a 100 realisations with generated aperture ensemble (b)

Table 1. KS test statistic for ensembles comprised of increasing number of aperture realisations tested against the 5% filtered measured aperture

No. of realisations	KS statistic
10	0.043
20	0.056
50	0.035
100	0.034

375 There is a significant spread in Hurst and scaling parameters, and which differs slightly
 376 between the upper and lower surfaces (Figure 7a,b). The Hurst exponent ranges from
 377 approximately 0.6 to 1 for both the upper and lower surface but a larger difference be-
 378 tween the surfaces is seen in the scaling parameter, which ranges from 0.025 to 0.06 and
 379 0.025 to 0.07 for the upper and lower surfaces respectively. The 25th, median and 75th
 380 percentiles have been calculated for both Hurst exponent and scaling parameter (Table
 381 2). The input parameters from the 75th percentiles generate an aperture ensemble dis-
 382 tribution that corresponds well with the measured aperture field scans, better than us-
 383 ing the median, and the 25th percentile showing the most dissimilar distribution (Fig-
 384 ure 7c). However, note that any of the parameter combinations plotted could be used
 385 for aperture generation, so the combination that produces an ensemble most similar to
 386 the aperture data must be determined.

387 3.2 Parameter sensitivity analysis

388 The analysis of the fracture scans yields a wide range of values for the Hurst ex-
 389 ponent and scaling parameter (Figure 7 and Table 2). Here we present an analysis of these
 390 parameter combinations in terms of their impact on the resulting generated aperture field
 391 distribution. A regular grid of points across the parameter space is considered, which
 392 has the advantage of providing a systematic analysis for regions both covered by the pair-
 393 wise correlated Hurst and scaling parameters as well as regions beyond. Each pair of Hurst
 394 exponent and scaling parameter in the grid is used to generate 100 realisations of the
 395 aperture field, and the ensemble evaluated against the measured aperture distribution.
 396 The similarity of the generated ensembles with the measured aperture was assessed us-
 397 ing the Kolmogorov–Smirnov (KS) test statistic, which measures the largest difference
 398 between the distributions of the two samples. Figure 8 shows an overlay of the KS statis-
 399 tic value, where a smaller value means a better fit between the distributions, on the reg-

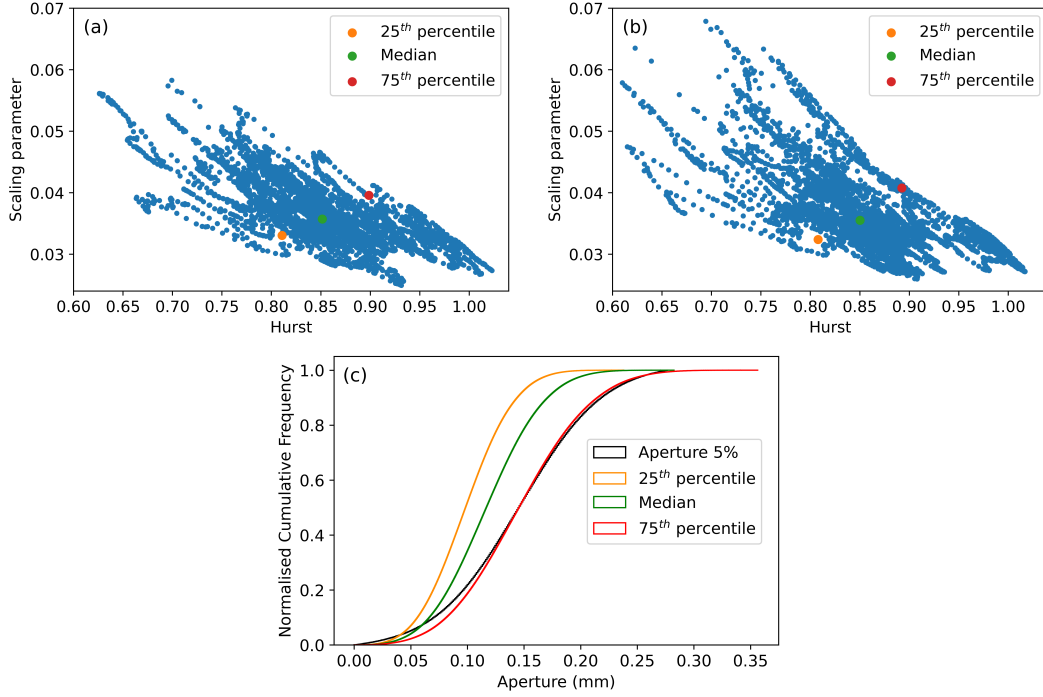


Figure 7. Hurst exponent and scaling parameter from each trace profiles along X and Y directions for the upper (a) and lower (b) surfaces and the corresponding cumulative distribution of the aperture ensembles using the 25th, median and 75th percentiles as input parameters (c)

Table 2. The 25th, median and 75th percentiles for Hurst exponent and scaling parameters for the upper and lower surfaces using different maximum step lengths in the RMS-COR function

Upper surface	Step length 20%		Step length 10%		Step length 5%	
	Hurst	Scaling	Hurst	Scaling	Hurst	Scaling
25 th percentile	0.660	0.040	0.811	0.033	0.875	0.030
Median	0.755	0.046	0.851	0.036	0.913	0.032
75 th percentile	0.822	0.057	0.899	0.040	0.947	0.034
Lower surface	Step length 20%		Step length 10%		Step length 5%	
	Hurst	Scaling	Hurst	Scaling	Hurst	Scaling
25 th percentile	0.653	0.040	0.808	0.032	0.873	0.029
Median	0.747	0.047	0.850	0.036	0.913	0.031
75 th percentile	0.817	0.057	0.892	0.041	0.951	0.035

400 ular grid parameter points over the scatter plots of parameters on the upper and lower
 401 surfaces. A linear regression was plotted using the weighted overlay to follow the trend
 402 of best fits (Figure 8, black line) which generally follows the upper bound of the param-
 403 eters. Moving away from this trend results in an increase in the KS statistic value as the

404 parameter combinations generate apertures that are less similar to the measured aper-
 405 ture. The 75th percentile combination for the Hurst and scaling parameter is very close
 406 to the linear regression line, and the ensemble generated using these values has the small-
 407 est KS statistic value. Therefore these values are used as input parameters for the final
 408 aperture generations.

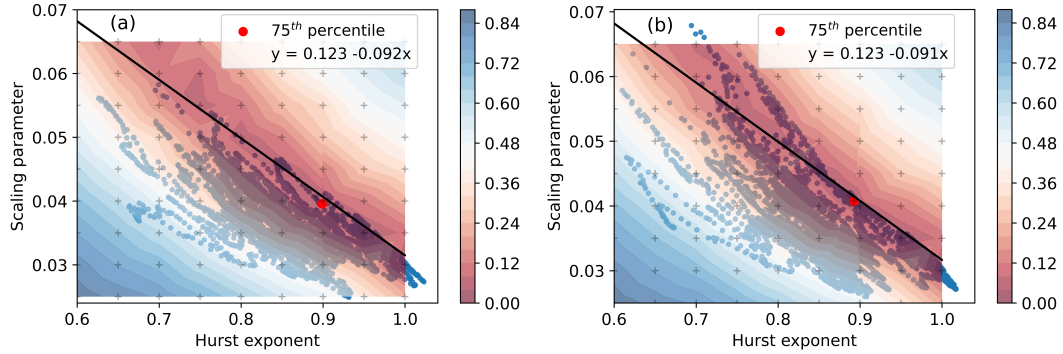


Figure 8. Hurst exponent and scaling parameter scatter plot overlain with fitting metric results for the upper (a) and lower (b) surfaces with the 75th percentile highlighted and regression line plotted using the weighted overlay

409 Figure 9a shows the correlation obtained from a polynomial fit which we propose
 410 here (red line) compared against the correlation obtained using the approach suggested
 411 by Ogilvie et al. (2006) (blue line). It can be seen that our approach has a lower gra-
 412 dient of change from low to high correlation, meaning that at larger wavelengths the sur-
 413 faces are not as strongly correlated as they would be compared to the approach by Ogilvie
 414 et al. (2006). The main difference is that the approach we suggest uses all of the infor-
 415 mation obtained from the PSDR analysis of the fracture scan sample; it does not solely
 416 rely on end points of the correlation and length over which the transition occurs. By in-
 417 troducing the polynomial fit of the PSDR, the generated aperture ensemble distribution
 418 is improved and better corresponds with the measured fracture sample (Figure 9b).

419 Box plots for the filtered aperture show the aperture ensemble generated using the
 420 Ogilvie et al. (2006) method and the new model developed in this paper (Figure 9c). This
 421 shows that the Ogilvie et al. (2006) method under predicts the distribution, with each
 422 of the values being lower than the filtered aperture data. However, the new model has
 423 a distribution that is very similar; the median value is only 0.001 mm smaller, with the
 424 biggest difference seen in the upper whiskers which are 0.013 mm larger.

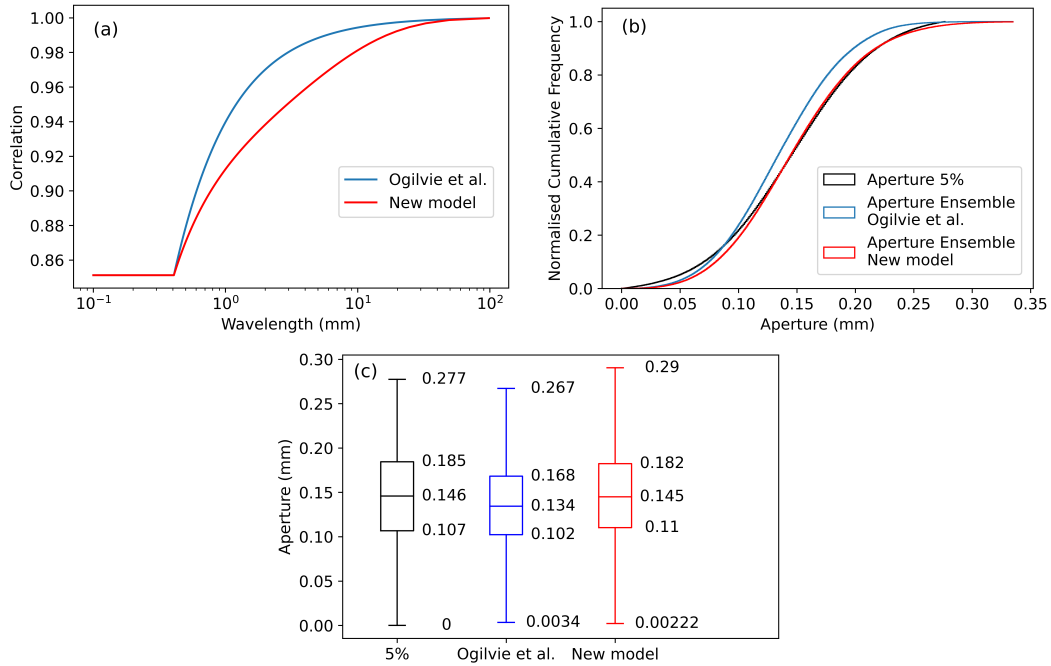


Figure 9. Comparison of Ogilvie method and the new model correlation with wavelength (a), aperture ensemble distribution generated from the new correlation and input parameters (b) and box plots of the 5% filtered aperture, Ogilvie method and new model ensemble (c)

4 Discussion

4.1 Field data filtering

During opening of the fracture some rock was broken off (Figure 2a), and although the volume of this debris is unknown it could be the cause of isolated and abnormally large apertures seen in the unfiltered distribution (cf. Figure 3a). The shape of some of the debris has similar geometry to the larger apertures, which further suggests that rock fall out is the cause. This is highlighted by red, black, purple and pink circles around rock debris and the possible location on the aperture field. The red, purple and pink circle encompass rock pieces that have a distinct shape, which seems to also be present in the aperture field and also in the pressure film data (Figure 2b,c). If the rock debris would have remained intact in these locations, the corresponding apertures would be significantly smaller. However, it is difficult to predict how adding the rock pieces would affect the apertures. For this reason, the aperture data has been filtered to remove the largest 5% of apertures, which should correct for the rock fallout and provide a more accurate representation of the distribution of the aperture when it was unopened. However, excessive filtering increases the risk of unintentional removal of large natural fracture apertures. We determined the threshold limit of 5% to be a reasonable balance without excessively impacting the overall shape of the aperture distribution (cf. Figure 3).

Another piece of rock fallout that visually fits well is highlighted by a black circle. This location represents a contact area, which is due to the subtraction of the lower surface scan from the upper resulting in a negative aperture, hence it is corrected to zero. It is not intuitive how additional rock mass would correct this, however from the pressure film data there is also a large void space at this location. This suggests that the rock piece was loosely attached during scanning, but has fallen off before the pressure film measurements were taken. If the piece was attached then a higher pressure would be ex-

450 pected, representing close contact, however it can be seen there is a void space at this
 451 location (Figure 2, black circle). This highlights further that great care should be taken
 452 when using the pressure film to vertically align the surfaces, as the 3D scan data and pres-
 453 sure film may not represent exactly the same state of the surfaces and resulting aper-
 454 ture field.

455 4.2 Hurst exponent and scaling parameter space

456 The spread of Hurst exponent and scaling parameter is in part due to the maxi-
 457 mum step length that is used when calculating RMS-COR function. Figure 10a,b shows
 458 the spread of parameters using a step length of 20%, 10% and 5% (orange, blue and green
 459 respectively) of the maximum trace length. Reducing the step length reduces the like-
 460 lihood of the regression line curving in log-log space, and hence reduces the spread (Marsch
 461 & Fernandez-Steeger, 2021). It should be noted that changing the step length has no ef-
 462 fect on the total number of Hurst and scaling values as the same number of trace pro-
 463 files are used. When a maximum step length of 20% is used the spread is large, rang-
 464 ing from approximately 0.35 to over 1 for the Hurst exponent. Small Hurst exponents
 465 seen in this range are not likely to be seen on fracture surfaces, as generally the Hurst
 466 exponent will range from 0.5 to 1 (S. Brown, 1987). As Hurst exponent decreases, it can
 467 be seen that some values of scaling parameter and Hurst exponent create a trend away
 468 from the main bulk of the scatter plot. This can most clearly be seen for a maximum
 469 step length of 20% at the lower Hurst exponent values. Potentially this could be due to
 470 trace profiles that go over sections where substantial parts of rock surface have fallen out
 471 during opening, which may perturb the assumption of the fractal nature of the fractures.
 472 Reducing the step lengths reduces the spread of these data away from the main bulk of
 473 the scatter plot, reducing errors that have been introduced from a larger step length. This
 474 reduction also decreases the extent by which the scatter plot data goes above the lin-
 475 ear regression that represents a line along which parameter combinations produce the
 476 best correspondence between aperture ensemble distributions and the measured aper-
 477 ture.

478 For the upper surface it is only the data obtained from a maximum step length of
 479 20% that has a significant amount of values above the regression line, with the other two
 480 data sets mostly staying below this line. This shows that for the upper surface the best
 481 parameter combinations fall on the upper bound of the data. For the lower surface this
 482 is not so obvious, as regardless of the step length, some of the parameter combinations
 483 fall above the linear regression. The Hurst exponent at which the values go above the
 484 linear regression decreases as the maximum step length increases. However for smaller
 485 step lengths, the majority of the data points stay below the linear regression line, sug-
 486 gesting the influence of rock fall out is also present in the lower surface. Table 2 shows
 487 the affect of maximum trace length on the 25th, median and 75th percentiles for Hurst
 488 exponent and scaling parameter.

489 When the maximum step length of 10% is used, the 75th percentile is on the up-
 490 per bound of the data for both the upper and lower surface, which also is very close to
 491 the regression line that represents the parameter combinations that produce the best aper-
 492 ture ensembles (Figure 10c,d). When the step length is reduced further to 5% then 75th
 493 percentile is slightly further away, but would still produce reasonably good aperture en-
 494 sembles. However, if a larger maximum step length is used then this value moves sig-
 495 nificantly above the regression line, which is seen for the maximum step length of 20%
 496 and would not produce an aperture ensemble that corresponds well with the measured
 497 aperture. This shows that a maximum step length of 10% is best when the full surface
 498 is used to obtain the 75th percentile parameter combination. This percentile lies on the
 499 upper bound of the data and is easy to calculate, making it easy to find this parame-
 500 ter combination as the input. However, any parameter combination along the linear re-
 501 gression line could be used as the input and produce an aperture ensemble that corre-

502 sponds with the measured aperture. The surfaces will have different topographies, but
 503 the resulting aperture distributions will be consistent. The regression line could represent
 504 a natural upper limit of the surface roughness, where values along this line best represent
 505 that specific surface. Hence, different rock and fracture types with different properties
 506 may have a different gradient to the line of regression.

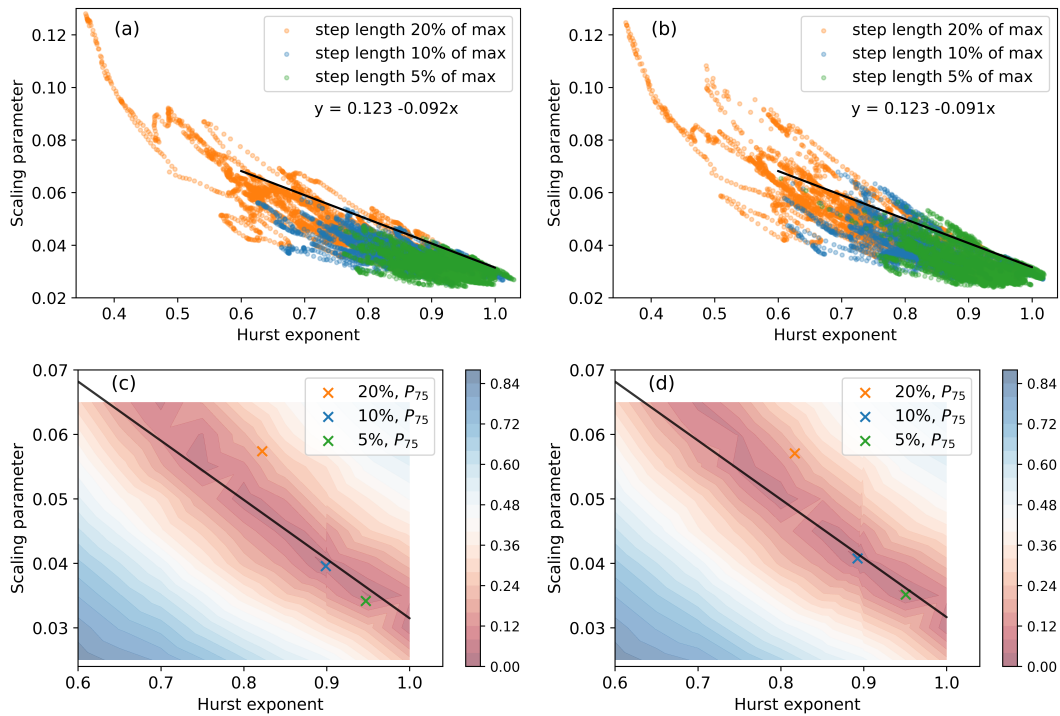


Figure 10. Upper (a) and lower (b) surface Hurst and scaling parameters for 20%, 10% and 5% of the maximum step length and regression line calculated from best fit overlay. The 75th percentiles for a maximum step length of 20%, 10% and 5% for the upper (c) and lower (d) surfaces and the linear regression line following the best fits

507 The method used to calculate Hurst exponent and scaling parameters used in this
 508 study is different from Ogilvie et al. (2006) as they used the slope of power spectral density
 509 to obtain these parameters. However, using the power spectral density to obtain input
 510 parameters can be affected more greatly by rock fall out which creates areas that
 511 are no longer self-affine. When used to calculate the Hurst exponent from these surfaces
 512 the result is a value of 0.52, compared to approximately 0.9 which is the 75th percentile
 513 value of the method we use. This could have worked for Ogilvie et al. (2006) as the frac-
 514 tures used in that study were artificially induced, therefore there was not the issue of forc-
 515 ing the fracture open and damaging the surfaces in the process to produce rock fall out.
 516 Since the fracture in this study is natural, using many traces across the surface and the
 517 RMS-COR evaluation method works better. This also allows the values which are most
 518 representative of the surface to be selected, as well as allowing the scaling parameter to
 519 be obtained from the same method.

520 This method can also work on fracture trace profiles, if the full surface is not avail-
 521 able for analysis. The correlation can be obtained from this data, but only one set of par-
 522 ameter combinations will be obtained, meaning the 75th percentile is unknown. In this
 523 case a maximum step length of 5% is best, as the spread of data is reduced (Figure 10a,b),

524 so it more likely that the Hurst and scaling parameter will be close to the best fit regres-
 525 sion line.

526 4.3 Upper and lower surface correlation

527 The model for aperture generation presented in this work has updated the method
 528 in which the correlation with scale changes. The PSDR is used, as it is in Ogilvie et al.
 529 (2006), but each wavenumber is used, which avoids the need to calculate a linear change
 530 between minimum and maximum correlation between the surfaces. Instead we can plot
 531 a polynomial regression through the PSDR (Figure 4) and base the correlation for each
 532 wavenumber off this, giving a more realistic transition from low to high correlation be-
 533 tween the surfaces as the scale changes. Depending on the order of polynomial however,
 534 it might not capture all the fluctuations. For example, as the correlation decreases with
 535 increasing wavenumber (decreasing scale) there are small fluctuations around wavenum-
 536 ber 9 (Figure 4). The fluctuations could be a result of large isolated apertures, as this
 537 wavenumber is approximately equivalent to the distance between large apertures, and
 538 could lead to the spike in the power spectral density that is observed. This fluctuation
 539 is not however captured in the correlation if a low order polynomial is used.

540 A sensitivity analysis of the aperture generation model to correlation with scale was
 541 tested using several different order polynomial regression fits. As can be seen from Fig-
 542 ure 11a,b using order 3, 9 and 16 has very little effect on the overall distribution. This
 543 suggests that it is the general trend that is more important to capture than every small
 544 fluctuation. The general trend captured from a third order polynomial regression is dif-
 545 ferent from the linear change that has been implemented in previous methods, and the
 546 improvements can be seen in Figure 9 where the update to correlation produces a gener-
 547 ated aperture ensemble distribution that highly corresponds with the measured aper-
 548 ture field.

549 Also, a synthetic analysis was conducted over an arbitrarily selected correlation with
 550 scale, but one that could be expected within reality (Figure 11c). Ten cases, each with
 551 a 100 fracture aperture realisations were systematically generated, with initially only wavenum-
 552 ber 1 correlated to the maximum value, increasing until the first 10 wavenumbers have
 553 a constant high correlation. After this point there is a decrease in correlation as the wavenum-
 554 bers increase as would be expected in a natural fracture. Distributions created with wavenum-
 555 bers 2 to 10 highly correlated are grouped together, and show no systematic change as
 556 the wavenumbers increase (Figure 11d). However when only wavenumber 1 is highly cor-
 557 related, it is clearly separate from the other distributions. This suggests that correlat-
 558 ing the first wavenumber correctly is more important than the following wavenumbers
 559 as the scale increases. Using a low order polynomial regression allows the first wavenum-
 560 ber to be accurately obtained while plotting the general trend of correlation for the fol-
 561 lowing wavenumbers, allowing an accurate representation of the aperture field to be pro-
 562 duced.

563 Although the large apertures have been filtered out when comparing the realisa-
 564 tions to the measured aperture, they are still present when calculating the PSDR and
 565 the correlation with scale. This may lead to slightly inaccurate correlation within the
 566 generated apertures. This could be corrected for if a reliable method for correcting sur-
 567 face scans is produced. However, currently there is no way to accurately digitally replace
 568 any rock fall out. To remove these areas during the matching analysis would also pro-
 569 duce errors with the correlation, most likely to an even greater extent. Errors from the
 570 matching analysis are a direct consequence of fall out during opening the fracture and
 571 scanning. Therefore it is imperative that this process be done as accurately as possible
 572 to allow for more accurate realisations of the aperture to be generated.

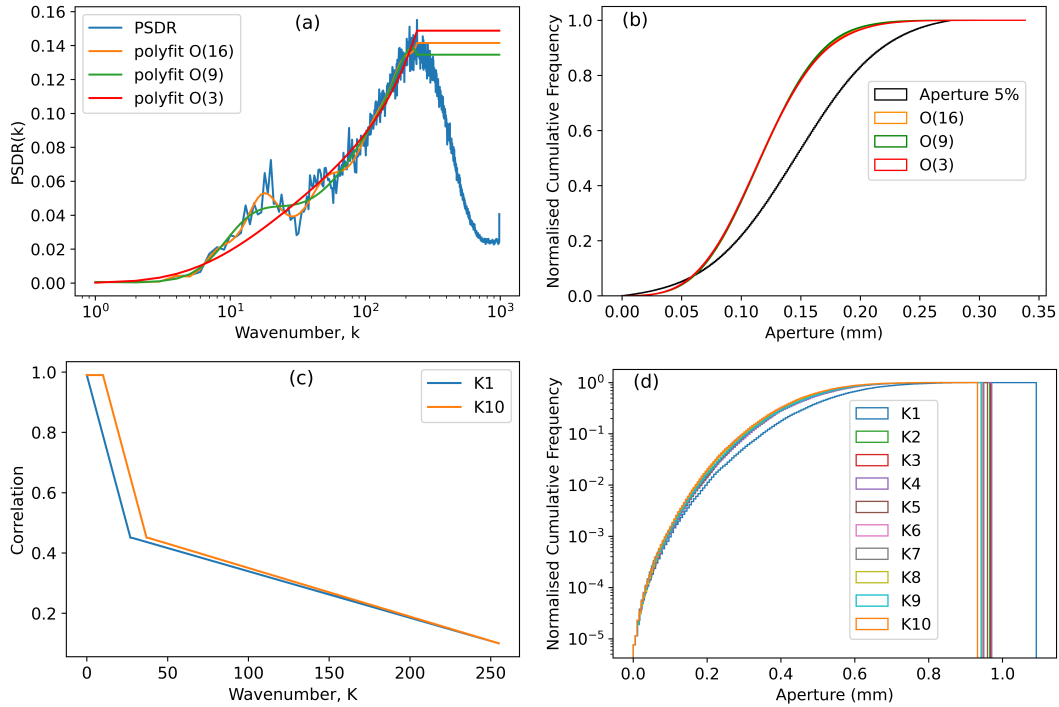


Figure 11. PSDR with different orders polynomial regression fits (a) and the resulting aperture distribution ensembles (b). Change in correlation with wavenumber for cases with the first wavenumber, K1, and the first 10 wavenumbers, K10, highly correlated (c) and the effects of increasing the amount of wavenumbers (K) that have the highest correlation on the aperture ensemble (d)

573

4.4 Implications for up-scaling

574

575

576

577

578

579

580

581

582

583

584

585

586

587

588

589

590

591

592

593

One reason for developing this method is to allow for representations of real fracture apertures to be up-scaled and implemented within larger scale DFNs. Figure 12a,b shows a scatter plot of Hurst exponent and scaling parameter for the full surface and a 100 mm^2 subsection. The linear regression represents the line along which the parameter combinations show the best correspondence with the measured aperture. As can be seen the 75th percentiles are situated close to the linear regression for parameters obtained from both sized sections, where blue represents the subsection and orange represents the full surface. For up-scaling the Hurst and scaling parameter should be selected from the upper bound of the data, and not a single value. The cropped section of the full surfaces has been used to generate an ensemble of 100 aperture realisations which have been up-scaled to $197 \times 197 \text{ mm}^2$, the results of which can be seen in Figure 12c,d. The difference between the median is 0.01 mm for the full aperture and 0.006 mm for the cropped aperture field. When the matching analysis is undertaken on the subsection, the correlation between the surfaces is slightly weaker, resulting in larger apertures when the up-scaled apertures are generated, leading to the difference in medians. However, overall the difference is only small and the ensemble corresponds moderately well with the measured aperture data, showing that this method can be used to up-scale aperture fields to any desired dimensions. Although this method does allow for up-scaling based solely on a fracture trace profile, it will not be as accurate as using a surface scan of the fracture surfaces.

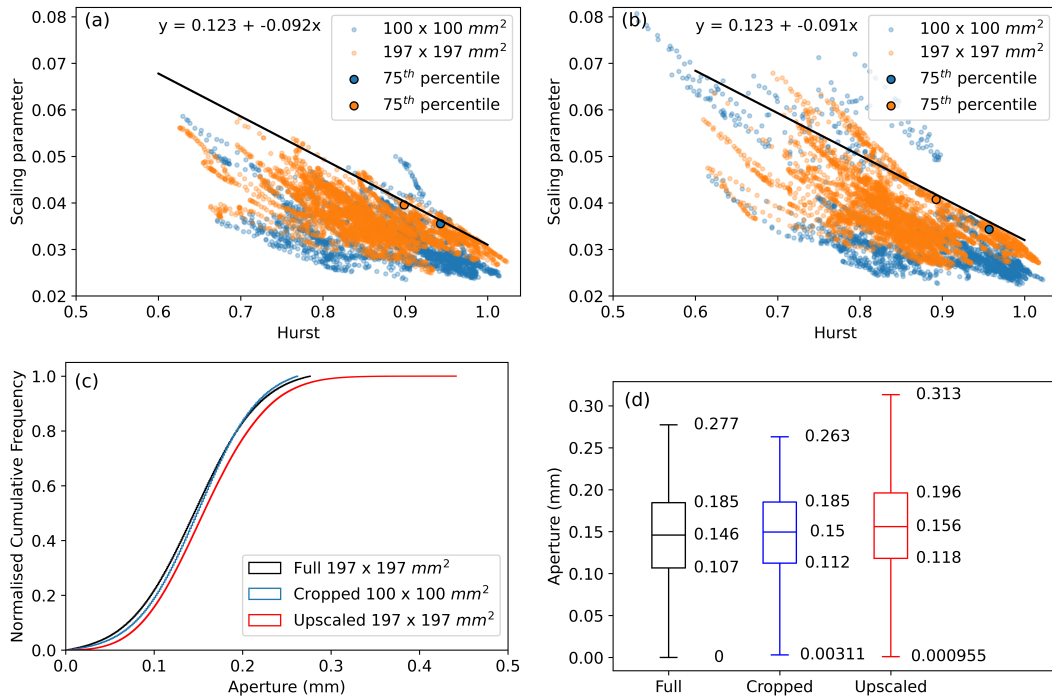


Figure 12. Hurst exponent and scaling parameter for the upper (a) and lower (b) surfaces with different dimensions, cumulative frequency of the full aperture, cropped and up-scaled aperture ensemble (c) and resulting box plots (d).

594 5 Conclusion

595 The method developed in this study can generate apertures that are representa-
 596 tive of natural rock fractures based on data from high resolution 3D fracture surface scans.
 597 During opening of the fracture, rock debris fell out, resulting in abnormally large aper-
 598 tures in the measured aperture distribution, which required filtering before comparison.
 599 The generated aperture ensemble distribution shows very high correspondence with the
 600 filtered measured aperture distribution. The approach to obtaining a correlation between
 601 upper and lower fracture surfaces has been improved based on previous methods by using
 602 a third order polynomial regression. This results in a general trend of change in cor-
 603 relation with scale which is implemented over the required wavenumbers. The changes
 604 in the minimum correlation at high wavenumbers can slightly affect the aperture distri-
 605 bution which can be seen from the up-scaled aperture realisations.

606 However it was found that fluctuations in correlation between the surfaces is not
 607 as sensitive as the input parameters that are used. The Hurst and scaling parameter are
 608 shown to exhibit a clear linear correlation, visible when plotted on a scatter plot; as the
 609 Hurst exponent increases the scaling parameter decreases. Reducing the maximum step
 610 length in the analysis of profile traces along the fracture surfaces reduces the spread of
 611 data and the number of outliers deviating away from the main trend.

612 Also, we show that using the 75th percentiles for the Hurst exponent and the scal-
 613 ing parameter result in aperture distributions that correspond very well with the mea-
 614 sured data. It was found that any parameter combination along a linear regression which
 615 follows the upper bound of correlation between the Hurst and scaling parameters would
 616 result in an aperture ensemble with high correspondence with the measured data. It is
 617 suggested that this upper bound could represent a natural upper limit for this rock or

618 fracture type, and the gradient of this trend may change depending on different rock types
 619 and stress state under which the fracture was induced. This method does not solely rely
 620 on full surface scans and can be readily used on surface profiles, in which case, the pa-
 621 rameter inputs should be obtained preferably with a relatively short maximum step length
 622 of 5%.

623 The way in which the surfaces are generated and the correlation between them, up-
 624 scaling of the generated apertures can be easily achieved. When the 75th percentiles for
 625 Hurst exponent and scaling parameter are calculated for a subsection of the full surfaces,
 626 the values are close to the linear regression calculated for the full surface. These values
 627 and the correlation between upper and lower surfaces of the subsection were successfully
 628 used to generate up-scaled aperture fields representing the full surface with moderately
 629 high correspondence. Aperture fields generated using this method are representative of
 630 natural fracture apertures and could be used for modelling larger fractures or multiple
 631 fractures, allowing for large scale discrete fracture network simulations to include realis-
 632 tic representation of aperture internal heterogeneity.

633 6 Data availability statement

634 The fracture surface data used for supporting the results presented in this paper
 635 are openly available from <https://doi.org/10.5281/zenodo.8354914> (Stock, 2023).

636 Acknowledgments

637 B. S. and A. F. gratefully acknowledge funding from the Swedish Nuclear Fuel and Waste
 638 Management Co. (SKB) and the Rock Engineering Research Foundation (BeFo).

639 References

- 640 Brown, S. (1987). Fluid flow through rock joints: The effect of surface rough-
 641 ness. *Journal of Geophysical Research: Solid Earth*. Retrieved 2020-08-31,
 642 from [https://agupubs.onlinelibrary.wiley.com/doi/abs/10.1029/
 643 JB092iB02p01337?casa_token=tRmMqdF21RoAAAAA:xztBT0RA4hXEgMe_Vx
 644 _z94i2XHXTsnCbhKnfCwChe1n7BV5zMsvcTCQN82UPQCLQTBavAW4mfiiuu6DU](https://agupubs.onlinelibrary.wiley.com/doi/abs/10.1029/JB092iB02p01337?casa_token=tRmMqdF21RoAAAAA:xztBT0RA4hXEgMe_Vx_z94i2XHXTsnCbhKnfCwChe1n7BV5zMsvcTCQN82UPQCLQTBavAW4mfiiuu6DU)
- 645 Brown, S. R. (1995a). Measuring the Dimension of Self-Affine Fractals: Example
 646 of Rough Surfaces. In C. C. Barton & P. R. La Pointe (Eds.), *Fractals in the*
 647 *Earth Sciences* (pp. 77–87). Boston, MA: Springer US. Retrieved 2022-11-
 648 10, from https://doi.org/10.1007/978-1-4899-1397-5_4 doi: 10.1007/978
 649 -1-4899-1397-5_4
- 650 Brown, S. R. (1995b). Simple mathematical model of a rough fracture. *Journal of*
 651 *Geophysical Research: Solid Earth*, 100(B4), 5941–5952. Retrieved 2021-10-
 652 05, from <https://onlinelibrary.wiley.com/doi/abs/10.1029/94JB03262>
 653 (_eprint: <https://onlinelibrary.wiley.com/doi/pdf/10.1029/94JB03262>) doi:
 654 10.1029/94JB03262
- 655 Brown, S. R. (1998). *Experimental observation of fluid flow channels in a*
 656 *single fracture - Brown - 1998 - Journal of Geophysical Research: Solid*
 657 *Earth - Wiley Online Library*. Retrieved 2020-08-31, from [https://
 658 agupubs.onlinelibrary.wiley.com/doi/abs/10.1029/97JB03542](https://agupubs.onlinelibrary.wiley.com/doi/abs/10.1029/97JB03542)
- 659 Brown, S. R., & Scholz, C. H. (1985). Closure of random elastic surfaces
 660 in contact. *Journal of Geophysical Research: Solid Earth*, 90(B7),
 661 5531–5545. Retrieved 2022-05-24, from [https://onlinelibrary
 662 .wiley.com/doi/abs/10.1029/JB090iB07p05531](https://onlinelibrary.wiley.com/doi/abs/10.1029/JB090iB07p05531) (_eprint:
 663 <https://onlinelibrary.wiley.com/doi/pdf/10.1029/JB090iB07p05531>) doi:
 664 10.1029/JB090iB07p05531
- 665 Bruines, P. (2022). *Description of Task 10.2 - Channelling in a single fracture*.

- 666 *Task 10 of SKB Task Force GWFTS - Validation approaches for groundwa-*
 667 *ter flow and transport modelling with discrete features. SKB P-22-06, Svensk*
 668 *Kärnbränslehantering AB.*
- 669 Cacas, M. C., Ledoux, E., Marsily, G. d., Tillie, B., Barbreau, A., Durand, E., ...
 670 Peaudecerf, P. (1990). Modeling fracture flow with a stochastic discrete frac-
 671 ture network: calibration and validation: 1. The flow model. *Water Resources*
 672 *Research*, 26(3), 479–489. Retrieved 2020-09-17, from [https://agupubs](https://agupubs.onlinelibrary.wiley.com/doi/abs/10.1029/WR026i003p00479)
 673 [.onlinelibrary.wiley.com/doi/abs/10.1029/WR026i003p00479](https://agupubs.onlinelibrary.wiley.com/doi/abs/10.1029/WR026i003p00479) (_eprint:
 674 <https://agupubs.onlinelibrary.wiley.com/doi/pdf/10.1029/WR026i003p00479>)
 675 doi: 10.1029/WR026i003p00479
- 676 Candela, T., Renard, F., Bouchon, M., Brouste, A., Marsan, D., Schmittbuhl, J., &
 677 Voisin, C. (2009, October). Characterization of Fault Roughness at Various
 678 Scales: Implications of Three-Dimensional High Resolution Topography Mea-
 679 surements. *Pure and Applied Geophysics*, 166(10-11), 1817–1851. Retrieved
 680 2021-06-02, from <http://link.springer.com/10.1007/s00024-009-0521-2>
 681 doi: 10.1007/s00024-009-0521-2
- 682 Durham, W. B., & Bonner, B. P. (1994). Self-propping and fluid flow in
 683 slightly offset joints at high effective pressures. *Journal of Geophysical*
 684 *Research: Solid Earth*, 99(B5), 9391–9399. Retrieved 2020-04-24, from
 685 <https://agupubs.onlinelibrary.wiley.com/doi/abs/10.1029/94JB00242>
 686 (_eprint: <https://agupubs.onlinelibrary.wiley.com/doi/pdf/10.1029/94JB00242>)
 687 doi: 10.1029/94JB00242
- 688 Frampton, A., & Cvetkovic, V. (2011). Numerical and analytical model-
 689 ing of advective travel times in realistic three-dimensional fracture net-
 690 works. *Water Resources Research*, 47(2). Retrieved 2022-04-05, from
 691 <https://onlinelibrary.wiley.com/doi/abs/10.1029/2010WR009290>
 692 (_eprint: <https://onlinelibrary.wiley.com/doi/pdf/10.1029/2010WR009290>)
 693 doi: 10.1029/2010WR009290
- 694 Frampton, A., Hyman, J. D., & Zou, L. (2019). Advective Transport in
 695 Discrete Fracture Networks With Connected and Disconnected Tex-
 696 tures Representing Internal Aperture Variability. *Water Resources*
 697 *Research*, 55(7), 5487–5501. Retrieved 2022-04-05, from [https://](https://onlinelibrary.wiley.com/doi/abs/10.1029/2018WR024322)
 698 onlinelibrary.wiley.com/doi/abs/10.1029/2018WR024322 (_eprint:
 699 <https://onlinelibrary.wiley.com/doi/pdf/10.1029/2018WR024322>) doi:
 700 10.1029/2018WR024322
- 701 Gallant, J. C., Moore, I. D., Hutchinson, M. F., & Gessler, P. (1994, May). Estimat-
 702 ing fractal dimension of profiles: A comparison of methods. *Mathematical Ge-*
 703 *ology*, 26(4), 455–481. Retrieved 2022-09-01, from [https://doi.org/10.1007/](https://doi.org/10.1007/BF02083489)
 704 [BF02083489](https://doi.org/10.1007/BF02083489) doi: 10.1007/BF02083489
- 705 Glover, P. W. J., Matsuki, K., Hikima, R., & Hayashi, K. (1998a). Fluid
 706 flow in synthetic rough fractures and application to the Hachimantai
 707 geothermal hot dry rock test site. *Journal of Geophysical Research:*
 708 *Solid Earth*, 103(B5), 9621–9635. Retrieved 2022-02-15, from [https://](https://onlinelibrary.wiley.com/doi/abs/10.1029/97JB01613)
 709 onlinelibrary.wiley.com/doi/abs/10.1029/97JB01613 (_eprint:
 710 <https://onlinelibrary.wiley.com/doi/pdf/10.1029/97JB01613>) doi: 10.1029/
 711 97JB01613
- 712 Glover, P. W. J., Matsuki, K., Hikima, R., & Hayashi, K. (1998b). Syn-
 713 thetic rough fractures in rocks. *Journal of Geophysical Research: Solid*
 714 *Earth*, 103(B5), 9609–9620. Retrieved 2022-11-10, from [https://](https://onlinelibrary.wiley.com/doi/abs/10.1029/97JB02836)
 715 onlinelibrary.wiley.com/doi/abs/10.1029/97JB02836 (_eprint:
 716 <https://onlinelibrary.wiley.com/doi/pdf/10.1029/97JB02836>) doi: 10.1029/
 717 97JB02836
- 718 Hakami, E. (1995). *Aperture distribution of rock fractures* (Tech. Rep. Nos. KTH-
 719 AMI-PHD-1003). Royal Inst. of Tech. Retrieved 2020-07-30, from [http://](http://inis.iaea.org/Search/search.aspx?orig_q=RN:27020199)
 720 inis.iaea.org/Search/search.aspx?orig_q=RN:27020199

- 721 Hurst, H. E. (1951, January). Long-Term Storage Capacity of Reservoirs.
 722 *Transactions of the American Society of Civil Engineers*, 116(1), 770–799.
 723 Retrieved 2022-09-01, from [https://ascelibrary.org/doi/10.1061/](https://ascelibrary.org/doi/10.1061/TACEAT.0006518)
 724 TACEAT.0006518 (Publisher: American Society of Civil Engineers) doi:
 725 10.1061/TACEAT.0006518
- 726 Isakov, E., Ogilvie, S. R., Taylor, C. W., & Glover, P. W. J. (2001, September).
 727 Fluid flow through rough fractures in rocks I: high resolution aperture deter-
 728 minations. *Earth and Planetary Science Letters*, 191(3), 267–282. Retrieved
 729 2023-01-03, from [https://www.sciencedirect.com/science/article/pii/](https://www.sciencedirect.com/science/article/pii/S0012821X01004241)
 730 S0012821X01004241 doi: 10.1016/S0012-821X(01)00424-1
- 731 Keller, A. A., Roberts, P. V., & Blunt, M. J. (1999). Effect of fracture
 732 aperture variations on the dispersion of contaminants. *Water Re-*
 733 *sources Research*, 35(1), 55–63. Retrieved 2023-01-03, from [https://](https://onlinelibrary.wiley.com/doi/abs/10.1029/1998WR900041)
 734 onlinelibrary.wiley.com/doi/abs/10.1029/1998WR900041 (_eprint:
 735 <https://onlinelibrary.wiley.com/doi/pdf/10.1029/1998WR900041>) doi:
 736 10.1029/1998WR900041
- 737 Lang, P. S., Paluszny, A., & Zimmerman, R. W. (2014). Permeability ten-
 738 sor of three-dimensional fractured porous rock and a comparison to
 739 trace map predictions. *Journal of Geophysical Research: Solid Earth*,
 740 119(8), 6288–6307. Retrieved 2020-09-12, from [https://agupubs](https://agupubs.onlinelibrary.wiley.com/doi/abs/10.1002/2014JB011027)
 741 [.onlinelibrary.wiley.com/doi/abs/10.1002/2014JB011027](https://agupubs.onlinelibrary.wiley.com/doi/abs/10.1002/2014JB011027) (_eprint:
 742 <https://agupubs.onlinelibrary.wiley.com/doi/pdf/10.1002/2014JB011027>) doi:
 743 10.1002/2014JB011027
- 744 Malinverno, A. (1990). A simple method to estimate the fractal dimen-
 745 sion of a self-affine series. *Geophysical Research Letters*, 17(11),
 746 1953–1956. Retrieved 2021-11-29, from [https://onlinelibrary](https://onlinelibrary.wiley.com/doi/abs/10.1029/GL017i011p01953)
 747 [.wiley.com/doi/abs/10.1029/GL017i011p01953](https://onlinelibrary.wiley.com/doi/abs/10.1029/GL017i011p01953) (_eprint:
 748 <https://onlinelibrary.wiley.com/doi/pdf/10.1029/GL017i011p01953>) doi:
 749 10.1029/GL017i011p01953
- 750 Mandelbrot, B. (1982). *The Fractal Geometry of Nature* (Vol. 1). WH Freeman New
 751 York.
- 752 Marsch, K., & Fernandez-Steege, T. M. (2021, April). Comparative Evaluation
 753 of Statistical and Fractal Approaches for JRC Calculation Based on a Large
 754 Dataset of Natural Rock Traces. *Rock Mechanics and Rock Engineering*, 54(4),
 755 1897–1917. Retrieved 2021-11-24, from [http://link.springer.com/10.1007/](http://link.springer.com/10.1007/s00603-020-02348-0)
 756 s00603-020-02348-0 doi: 10.1007/s00603-020-02348-0
- 757 Nicholl, M. J., Rajaram, H., Glass, R. J., & Detwiler, R. (1999). Sat-
 758 urated flow in a single fracture: evaluation of the Reynolds Equa-
 759 tion in measured aperture fields. *Water Resources Research*,
 760 35(11), 3361–3373. Retrieved 2020-08-31, from [https://agupubs](https://agupubs.onlinelibrary.wiley.com/doi/abs/10.1029/1999WR900241)
 761 [.onlinelibrary.wiley.com/doi/abs/10.1029/1999WR900241](https://agupubs.onlinelibrary.wiley.com/doi/abs/10.1029/1999WR900241) (_eprint:
 762 <https://agupubs.onlinelibrary.wiley.com/doi/pdf/10.1029/1999WR900241>) doi:
 763 10.1029/1999WR900241
- 764 Novakowski, K. S., & Lapcevic, P. A. (1994). Field measurement of
 765 radial solute transport in fractured rock. *Water Resources Re-*
 766 *search*, 30(1), 37–44. Retrieved 2020-08-31, from [https://agupubs](https://agupubs.onlinelibrary.wiley.com/doi/abs/10.1029/93WR02401)
 767 [.onlinelibrary.wiley.com/doi/abs/10.1029/93WR02401](https://agupubs.onlinelibrary.wiley.com/doi/abs/10.1029/93WR02401) (_eprint:
 768 <https://agupubs.onlinelibrary.wiley.com/doi/pdf/10.1029/93WR02401>) doi:
 769 10.1029/93WR02401
- 770 Ogilvie, S. R., Isakov, E., & Glover, P. W. (2006, January). Fluid flow through
 771 rough fractures in rocks. II: A new matching model for rough rock frac-
 772 tures. *Earth and Planetary Science Letters*, 241(3-4), 454–465. Retrieved
 773 2021-10-05, from [https://linkinghub.elsevier.com/retrieve/pii/](https://linkinghub.elsevier.com/retrieve/pii/S0012821X05008174)
 774 S0012821X05008174 doi: 10.1016/j.epsl.2005.11.041
- 775 Ogilvie, S. R., Isakov, E., Taylor, C. W., & Glover, P. W. J. (2003, January).

- 776 Characterization of rough-walled fractures in crystalline rocks. *Geolog-*
 777 *ical Society, London, Special Publications, 214* (1), 125–141. Retrieved
 778 2023-01-03, from [https://www.lyellcollection.org/doi/abs/10.1144/](https://www.lyellcollection.org/doi/abs/10.1144/gsl.sp.2003.214.01.08)
 779 [gsl.sp.2003.214.01.08](https://www.lyellcollection.org/doi/abs/10.1144/gsl.sp.2003.214.01.08) (Publisher: The Geological Society of London) doi:
 780 10.1144/GSL.SP.2003.214.01.08
- 781 Power, W. L., & Tullis, T. E. (1991). Euclidean and fractal models for the
 782 description of rock surface roughness. *Journal of Geophysical Research:*
 783 *Solid Earth, 96*(B1), 415–424. Retrieved 2022-09-01, from [https://](https://onlinelibrary.wiley.com/doi/abs/10.1029/90JB02107)
 784 onlinelibrary.wiley.com/doi/abs/10.1029/90JB02107 (_eprint:
 785 <https://onlinelibrary.wiley.com/doi/pdf/10.1029/90JB02107>) doi: 10.1029/
 786 90JB02107
- 787 Power, W. L., & Tullis, T. E. (1992). The contact between opposing fault surfaces
 788 at Dixie Valley, Nevada, and implications for fault mechanics. *Journal of Geo-*
 789 *physical Research: Solid Earth, 97*(B11), 15425–15435. Retrieved 2022-02-15,
 790 from <https://onlinelibrary.wiley.com/doi/abs/10.1029/92JB01059>
 791 (_eprint: <https://onlinelibrary.wiley.com/doi/pdf/10.1029/92JB01059>) doi:
 792 10.1029/92JB01059
- 793 Renard, F., Voisin, C., Marsan, D., & Schmittbuhl, J. (2006). High res-
 794 olution 3D laser scanner measurements of a strike-slip fault quan-
 795 tify its morphological anisotropy at all scales. *Geophysical Re-*
 796 *search Letters, 33*(4). Retrieved 2021-09-15, from [https://](https://onlinelibrary.wiley.com/doi/abs/10.1029/2005GL025038)
 797 onlinelibrary.wiley.com/doi/abs/10.1029/2005GL025038 (_eprint:
 798 <https://agupubs.onlinelibrary.wiley.com/doi/pdf/10.1029/2005GL025038>) doi:
 799 10.1029/2005GL025038
- 800 Stigsson, M., & Mas Ivars, D. (2019, April). A Novel Conceptual Approach to Ob-
 801 jectively Determine JRC Using Fractal Dimension and Asperity Distribution
 802 of Mapped Fracture Traces. *Rock Mechanics and Rock Engineering, 52*(4),
 803 1041–1054. Retrieved 2021-05-26, from [http://link.springer.com/10.1007/](http://link.springer.com/10.1007/s00603-018-1651-6)
 804 [s00603-018-1651-6](http://link.springer.com/10.1007/s00603-018-1651-6) doi: 10.1007/s00603-018-1651-6
- 805 Stock, B. (2023, September). *Fracture surface data* [dataset]. Retrieved from
 806 <https://doi.org/10.5281/zenodo.8354914> doi: 10.5281/zenodo.8354914
- 807 Stock, B., & Frampton, A. (2022, June). Processing and Conversion of Raw Point-
 808 Cloud Laser Measurements and Auxiliary Data of Rough-Surfaced Fractures
 809 To Generate Corresponding Fracture Aperture Fields. OnePetro. Retrieved
 810 2023-05-16, from [https://onepetro.org/ARMADFNE/proceedings-abstract/](https://onepetro.org/ARMADFNE/proceedings-abstract/DFNE22/A11-DFNE22/515893)
 811 [DFNE22/A11-DFNE22/515893](https://onepetro.org/ARMADFNE/proceedings-abstract/DFNE22/A11-DFNE22/515893) doi: 10.56952/ARMA-DFNE-22-0020
- 812 Tsang, C.-F., & Neretnieks, I. (1998). Flow channeling in heterogeneous frac-
 813 tured rocks. *Reviews of Geophysics, 36*(2), 275–298. Retrieved 2022-08-24,
 814 from <https://onlinelibrary.wiley.com/doi/abs/10.1029/97RG03319>
 815 (_eprint: <https://onlinelibrary.wiley.com/doi/pdf/10.1029/97RG03319>) doi:
 816 10.1029/97RG03319
- 817 Witherspoon, P. A., Wang, J. S. Y., Iwai, K., & Gale, J. E. (1980). Validity of
 818 Cubic Law for fluid flow in a deformable rock fracture. *Water Resources*
 819 *Research, 16*(6), 1016–1024. Retrieved 2020-07-21, from [https://agupubs](https://agupubs.onlinelibrary.wiley.com/doi/abs/10.1029/WR016i006p01016)
 820 [.onlinelibrary.wiley.com/doi/abs/10.1029/WR016i006p01016](https://agupubs.onlinelibrary.wiley.com/doi/abs/10.1029/WR016i006p01016) (_eprint:
 821 <https://agupubs.onlinelibrary.wiley.com/doi/pdf/10.1029/WR016i006p01016>)
 822 doi: 10.1029/WR016i006p01016
- 823 Zimmerman, R. W., & Bodvarsson, G. S. (1996, April). Hydraulic conductivity of
 824 rock fractures. *Transport in Porous Media, 23*(1), 1–30. Retrieved 2019-11-11,
 825 from <https://doi.org/10.1007/BF00145263> doi: 10.1007/BF00145263
- 826 Zou, L., Jing, L., & Cvetkovic, V. (2017, September). Modeling of flow
 827 and mixing in 3D rough-walled rock fracture intersections. *Advances*
 828 *in Water Resources, 107*, 1–9. Retrieved 2021-06-14, from [https://](https://www.sciencedirect.com/science/article/pii/S0309170816305097)
 829 www.sciencedirect.com/science/article/pii/S0309170816305097 doi:
 830 10.1016/j.advwatres.2017.06.003

1 **Fracture aperture generation using surface scan**
2 **measurements of natural rock samples**

3 **Brandon Stock¹, Andrew Frampton^{1,2}**

4 ¹Department of Physical Geography, Stockholm University, Stockholm, Sweden

5 ²Bolin Center for Climate Research, Stockholm University, Stockholm, Sweden

6 **Key Points:**

- 7 • A model for aperture generation based on self-affine theory is improved and eval-
8 uated using surface scans of a natural rock sample
- 9 • A linear correlation between Hurst exponent and scaling parameter can accurately
10 reproduce the aperture distribution of the natural fracture
- 11 • The improved model is shown to successfully generate up-scaled aperture fields
12 using subsections of the natural rock surface

Corresponding author: Brandon Stock, Brandon.Stock@natgeo.su.se

Abstract

In sparsely fractured crystalline rock, aperture variability exhibits significant control of the flow field through the fracture network. However, its inclusion in models is hampered due to a lack of field measurements and adequate numerical representation. A model for aperture generation is developed based on self-affine methods which includes two key parameters, the Hurst exponent and a scaling parameter, and which accounts for relative anisotropy and correlation between the adjacent surfaces forming the fracture. A methodology for analysing and extracting the necessary parameters from 3D surface scans of natural rock fractures is also developed. Analysis of the Hurst exponent and scaling parameter space shows that input combinations following a linear upper bound can be used to generate aperture fields which accurately reproduce measurements. It is also shown that the Hurst and scaling parameters are more sensitive than the correlation between the upper and lower fracture surfaces. The new model can produce an aperture ensemble that closely corresponds with the aperture obtained from the surface scans, and is an improvement on previous methods. The model is also successfully used to up-scale fracture apertures based on measurements restricted to a small sub-section of the sample. Thereby, the aperture fields generated using the model are representative of natural fracture apertures and can be implemented in larger scale fracture network models, allowing for numerical simulations to include representation of aperture internal heterogeneity.

Plain Language Summary

Understanding fluid flow through naturally fractured rock is important for several applications, including subsurface infrastructure and storage of nuclear waste. Many studies assume fractures as smooth planes; however, it is known that real fractures have rough surfaces and a variable aperture, and this variability can significantly control water flow. It is difficult to include an accurate representation of aperture variability in models because of a lack of field measurements, as well as difficulties in creating adequate model-based representations of the variable aperture field. In this study, improvements are made to a previously developed approach for aperture generation, which is based on self-affine theory. The theory is founded on observations of fractal behaviour exhibited by rock surfaces. It is shown that parameter combinations that follow a linear upper bound can be used to generate aperture fields that accurately reproduce the measured apertures. The model is also successfully used to generate up-scaled aperture fields based on a subsection of the fracture sample. Aperture fields generated using this model are representative of natural fracture apertures and can be used in larger scale models, allowing for a realistic representation of aperture variability to be included when simulating flow in models for fractured rock.

1 Introduction

Understanding fluid flow through natural fractured rocks systems is important for several applications, including subsurface infrastructure, storage facilities for spent nuclear fuel and other toxic waste, and hydrocarbon industries (Tsang & Neretnieks, 1998). Flow and transport through sparsely fractured rock is often modelled using a discrete fracture network (DFN) approach because it is well-suited to numerically represent the typically complex geometries observed in fractured bedrock (Cacas et al., 1990; Framp-ton & Cvetkovic, 2011; Lang et al., 2014). Representation of fractures in DFN models is typically based on the parallel-plate assumption (Witherspoon et al., 1980; Zimmerman & Bodvarsson, 1996), where fracture permeability is often used to represent the aperture void space within fractures. However, DFN models often simplify the effect of internal aperture variability by assuming constant or effectively homogeneous hydraulic properties within the plane of individual fractures. Although most DFN models are able

63 to numerically include internal variability, its representation is hampered by a lack of
64 field measurements. Also, homogenisation allows for a computationally less demanding
65 description of the fluid flow between fractures, which simplifies run times for large DFNs.
66 Nonetheless, it is well known that fractures are rough walled conduits with varying aper-
67 ture and multiple contact points (Durham & Bonner, 1994; Novakowski & Lapcevic, 1994;
68 Hakami, 1995; S. R. Brown, 1998), and studies have shown that these features can ex-
69 hibit control of the flow field through both single fractures (S. Brown, 1987; Nicholl et
70 al., 1999; Zou et al., 2017) as well as fracture networks (Frampton et al., 2019).

71 Fracture surface roughness has been shown to exhibit self-affine fractal properties
72 (S. Brown, 1987; Power & Tullis, 1991; Renard et al., 2006). Self-affine differ from self-
73 similar fractals as they scale anisotropically along horizontal and vertical reference axes
74 whereas self-similar scale isotropically (Mandelbrot, 1982; Power & Tullis, 1991). The
75 fractal dimension, D , of the surface describes the complexity of the fractal (Malinverno,
76 1990; Power & Tullis, 1991), and the Hurst exponent, $H = E - D$ (Hurst, 1951), is a mea-
77 sure of the randomness, where E is the number of spatial dimensions in which the frac-
78 tal is measured. The values of D for rock fractures typically range from 1-1.5 for pro-
79 files and 2-2.5 for surfaces (S. Brown, 1987). This agrees with the definition of self-affine
80 fractals where $D = 1.5$ for profiles compared to self-similar definition where $D = 2$ (S. Brown,
81 1987). When describing fracture surfaces using fractals, the Hurst exponent is more con-
82 venient (Gallant et al., 1994).

83 Therefore, in order to generate fractures with internal variability, for example for
84 use in numerical DFN models for flow and transport, the methods used should preserve
85 the self-affine properties of the natural rough-surfaced fractures they aim to reproduce.
86 This includes the Hurst exponent and scaling parameter, but also surface height vari-
87 ability, relative anisotropy, and correlation between the upper and lower surfaces form-
88 ing the fracture aperture (Ogilvie et al., 2006). Another aspect to take into considera-
89 tion is the stochastic nature of aperture generation and its needs for numerical DFN mod-
90 elling. Typically, a large number of fractures are used in models, far more than can re-
91 alistically be sampled and studied from field investigation. Therefore it is desirable to
92 be able to generate multiple fractures based off of a limited set of fracture aperture mea-
93 surements, thereby using the same or small set of input parameters to generate multi-
94 ple fracture realisations (Isakov et al., 2001; Ogilvie et al., 2003). Furthermore, DFN mod-
95 els typically require fractures to be generated at multiple spatial scales, and often at a
96 much greater scale than available from measurements. Thus there is a practical need to
97 upscale fractures, and here, self-affine methods are well suited as spatial rescaling is in-
98 herent to their design.

99 Natural fractures are complex to replicate due to their anisotropy and the corre-
100 lation exhibited between the upper and lower rough surfaces forming the aperture void
101 space. A root-mean squared (RMS) correlation function has successfully been used to
102 characterise anisotropy on exposed structures (Candela et al., 2009). To obtain variable
103 aperture, two partially correlated rough surfaces are needed. Although generation of in-
104 dependent surfaces is relatively easy, correlation and separation between two surfaces is
105 needed for creating realistic fracture apertures. It is understood that correlation between
106 the surfaces is weak at short wavelengths, where the surface variabilities act reasonably
107 independently of each other, but becomes stronger, and reaches a peak, as wavelength
108 increases (S. Brown, 1987; S. R. Brown & Scholz, 1985; Keller et al., 1999; Ogilvie et al.,
109 2006). Surfaces have been found to be well correlated above the scale of a few millime-
110 tres (S. R. Brown & Scholz, 1985; Power & Tullis, 1992).

111 Several attempts have been made to represent the change in correlation with scale.
112 Previous work by S. R. Brown (1995b) proposed a second surface generated with a ‘mis-
113 match length scale’. The wavelengths for the mismatch were obtained from the power
114 spectral density ratio (PSDR). The surfaces are well-correlated at large wavelengths and
115 uncorrelated when the wavelength becomes less than the assigned mismatch length scale.

116 A set of random numbers can be used to define the phase of the Fourier components which
117 are used to generate the upper and lower surfaces. The correlation between the random
118 number set at different length scales therefore determines the correlation between sur-
119 faces of the generated aperture. S. R. Brown (1995b) implemented the uncorrelated length
120 scale by using a second random number generator different from the one used to pro-
121 duce the first surface. This decorrelates the surfaces at scales below the mismatch length,
122 and amplitudes for wavelengths greater than the mismatch length use the same num-
123 ber generator as the one used to create the first surface. This creates a sharp disconti-
124 nuity between correlated and uncorrelated surfaces. However, Glover et al. (1998b) ar-
125 gued that the transition should be smooth, following a frequency dependent change from
126 high to low correlation. The PSDR function of the surfaces combined with a weighting
127 function was suggested which determines the rate at which the surfaces match with re-
128 spect to frequency.

129 Glover et al. (1998b) required two independent random number sets for the wave-
130 lengths that are less than the mismatch wavelength, and above this the random num-
131 bers are partially correlated. This involved mixing sets of two random numbers using
132 linear weighting. However, Ogilvie et al. (2006) noted that algebraically mixing random
133 number sets in this manner breaks down the distribution produced by the random num-
134 ber generator. Therefore, they proposed an algorithm which swaps the positions of num-
135 bers in two random number sets until the desired correlation is reached, producing a par-
136 tially correlated random number data set. This has the advantage of maintaining the
137 distribution produced by the random number generator as well as enabling the corre-
138 lation to vary with scale between the two surfaces, producing a more accurate aperture.

139 Ogilvie et al. (2006) uses several parameters to determine how the matching be-
140 tween surfaces changes with scale based on the PSDR. These are an improvement on pre-
141 vious methods as a minimum and maximum matching fraction can be set and how the
142 change in correlation varies between these two points. However, the overall change from
143 low to high correlation is still a linear change, and even with added parameters to in-
144 crease the accuracy, it still may not represent natural fractures. That study was also per-
145 formed on synthetically induced mode I fractures; thus, it is not yet known how well these
146 methods perform when using measurements from and comparing against real-world nat-
147 ural rock fractures.

148 The aim of this study is to develop and evaluate a method for reproducing rough-
149 surfaced fractures with variable aperture using information obtained from 3D scans of
150 natural rock fracture surfaces. A model for stochastic fracture aperture generation is fur-
151 ther developed based on previous work using self-affine fractal concepts, which includes
152 a refined method for representing correlation between the upper and lower surfaces of
153 the fracture. The model is used to generate an ensemble of realisations of fracture aper-
154 tures, which is evaluated against the measured natural fracture aperture. Furthermore,
155 a detailed sensitivity analysis is conducted on the variability of the Hurst and scaling
156 parameters and the correlation obtained from the surface scans of the fracture in terms
157 of their impact on model performance. Finally, the model is evaluated in terms of spa-
158 tial up-scaling, where a subsection of the measurements are used to predict the full ex-
159 tent of the fracture.

160 2 Method

161 A spectral synthesis approach is used to numerically produce fractals that repre-
162 sent two surfaces which when combined form a fracture with variable aperture void space.
163 A symmetric matrix containing Fourier components is defined, where the Fourier com-
164 ponents can be obtained from measurements to obey the various desired properties of
165 the fracture. Each component is comprised of an amplitude and a phase. Fractal dimen-
166 sion and any information about relative anisotropy is contained within the amplitude

167 component that scales with a power law. Thus, the topography of the fracture surfaces
 168 are controlled by the phase of the Fourier components. If the phase is identical for the
 169 upper and lower surfaces, the resulting fracture aperture is constant, representing a per-
 170 fectly mated fracture. In order to create a variable aperture field, the topography of the
 171 two surfaces need to be uncorrelated or partially correlated at different wavelengths. When
 172 random numbers are used to describe the phase of the Fourier components, the degree
 173 of matedness between the surfaces can be controlled by the degree of correlation between
 174 the random numbers used.

175 Natural rock surfaces can be described by a power spectral density function (S. R. Brown,
 176 1995a),

$$177 \quad G(k) = Ck^{-\alpha} \quad (1)$$

178 where $k = 2\pi/\lambda$ is the wavenumber, λ is the wavelength which corresponds to distance
 179 along the profile, C is a proportionality constant which varies among surfaces and cor-
 180 responds to the intercept of the logarithm of the power spectrum, and α is the fractal
 181 dimension in the range of $2 < \alpha < 3$ which corresponds to the slope of the logarithm of
 182 the power spectrum. To obtain the correlation between the upper and lower surfaces of
 183 the fracture scans, the power spectral density (PSD) of each surface and the resulting
 184 aperture needs to be obtained, which can readily be calculated using Fast Fourier Trans-
 185 forms.

186 In principle the Fourier decomposition of a surface can be done for an infinite num-
 187 ber of wavenumbers k , however in practice there is a clear limit. The limit is defined by
 188 the resolution of the surface scans, and any pre-processing interpolation that has been
 189 done before calculating the PSD of the fracture surface. When the period of the sine waves
 190 are equal to the number of mesh cells in one dimension, then each oscillation of the sine
 191 wave exactly covers one cell. Increasing the resolution beyond this point so more sine
 192 waves cover a single cell would have no further effect on the amplitude. The maximum
 193 frequency that is useful for the surface is therefore $k = 1/N$, where N is the maximum
 194 number of cells along one edge length of the fracture scan. When $k = 1$ this corresponds
 195 to a sine wave that fits exactly once within the surface.

196 2.1 Correlation analysis

197 The correlation of the upper and lower fracture surfaces can be calculated by us-
 198 ing the ratio of the PSD from the aperture over the sum of the PSDs of the two surfaces;
 199 it is convenient to plot it as a function of wavelength on log-log scale. Ogilvie et al. (2006)
 200 called this the PSD Ratio (PSDR, $\xi(k)$), where

$$201 \quad \xi(k) = \frac{G(k)_{\text{aperture}}}{G(k)_{\text{upper surface}} + G(k)_{\text{lower surface}}} \quad (2)$$

202 If the PSD ratio tends towards unity for all wavenumbers then the surfaces are completely
 203 independent (Glover et al., 1998b, 1998a). If the PSDR is less than unity, then some match-
 204 ing correlation is occurring between the upper and lower fracture surfaces at that spe-
 205 cific wavenumber. The correlation at each wavenumber is obtained as $\text{Corr}(k) = 1 -$
 206 $\xi(k)$. Here we introduce a polynomial regression over the PSDR obtained from measure-
 207 ments of a rock fracture from the smallest to largest PSDR(k) value as a convenient ap-
 208 proach to remove the fluctuations and get values for the general trend as a function of
 209 wavenumber (or wavelength). Fluctuations in the PSDR inevitably occur when calcu-
 210 lating the PSD from measurements of fracture surfaces due to natural variability in the
 211 upper and lower surface as well as measurement precision.

212 During aperture generation, different quantities of wavenumbers may be required,
 213 and will not necessarily match the amount coming from the measurements of a real frac-
 214 ture. Therefore, the correlation values are typically re-scaled along the length direction
 215 of a profile to the correct number of values that are needed for the generation method.

216 Due to the method of generating a self-affine fractal surface, the dimensions are limited
 217 to $2 \times 2^n + 1$ in X and Y , so the correlation values are scaled in length to 2^n , which is
 218 half of the desired edge length of which the aperture will be generated at. This is im-
 219 portant as it will maintain the desired correlation and structure regardless of the reso-
 220 lution used to generate the aperture.

221 Fractures typically have high correlation at small wavenumbers (large wavelengths),
 222 indicating there is large-scale correlation across the fracture. As the wavenumber increases
 223 (and wavelength decreases) the matching between the surfaces typically decreases. Once
 224 the correlation function $\text{Corr}(k)$ is obtained, a number swapping algorithm is used to cre-
 225 ate several arrays of different correlation which represent the different wavenumbers. We
 226 adopted a method similar to Ogilvie et al. (2006), and developed a number swapping al-
 227 gorithm that swaps the positions of numbers within one random normally distributed
 228 array until a set correlation, defined by the matching analysis, is reached between the
 229 other random normally distributed array. The algorithm is executed several times such
 230 that two correlated arrays are created for every wavenumber that is needed. Correlated
 231 pairs of values are selected from the arrays and are placed in two grids that represent
 232 the upper and lower surface in the corrected position depending on the wavenumber. This
 233 creates a partial correlation between the upper and lower surface that changes with scale.
 234 To create different realisations different pairs are randomly selected from the arrays, and
 235 the phase of the Fourier components is defined by these random number sets.

236 2.2 Scaling properties

237 The other properties needed to generate a self-affine fractal surface are the Hurst
 238 exponent H and a scaling parameter. For a self-affine profile to appear similar at dif-
 239 ferent scales, it must be scaled anisotropically in two different directions, i.e., length ver-
 240 sus topographical height of a rough surface. If the abscissa (length) is scaled by a fac-
 241 tor of λ , the ordinate (height) needs to be scaled by λ^H . We adopt the RMS-COR method
 242 (Malinverno, 1990; Renard et al., 2006; Candela et al., 2009; Stigsson & Mas Ivars, 2019)
 243 to analyse the standard deviation of height difference at different length intervals; at ver-
 244 tices Δv apart the standard deviation σ of the height differences δh is obtained as:

$$245 \quad \sigma(\delta h(\Delta v)) = \sqrt{\frac{\sum_{v=0}^{N-\Delta v} (h(v + \Delta v) - h(v))^2}{N + 1 - \Delta v} - \left(\frac{\sum_{v=0}^{N-\Delta v} (h(v + \Delta v) - h(v))}{N + 1 - \Delta v} \right)^2} \quad (3)$$

246 where Δv is the number of vertices between the height values being analysed, $h(v)$ is the
 247 height value at vertex v , and N is the number of vertices within the line. The Hurst ex-
 248 ponent H is obtained by a log-log fit of the standard deviations σ against the distance
 249 between the vertices Δv ; the slope of the line corresponds to H and the intercept cor-
 250 responds to the standard deviation of adjacent vertices δh , the value which is used to
 251 scale generated surfaces.

252 The method is relatively easy to implement but affected by the finite length of trace
 253 profiles. Therefore, Δv must be small compared to N ; for this reason if Δv is above ap-
 254 proximately 10% of maximum trace length it is not considered reliable (Marsch & Fernandez-
 255 Steeger, 2021). The Hurst exponent can also be underestimated due to the finite trace
 256 length. However, the RMS-COR method is considered to under-estimate Hurst expo-
 257 nents when $H > 0.5$ (Stigsson & Mas Ivars, 2019). Therefore, we implement the fol-
 258 lowing correction as suggested by Marsch and Fernandez-Steeger (2021); if $H_{RMS,cal} >$
 259 0.5 then $H_{RMS} = \ln(H_{RMS,cal}) + 1.18$.

2.3 Surface scans of a natural fracture

The rock sample was taken from a medium grained granite block from the Flivik quarry in Oskarshamn municipality, Sweden, and includes a natural vertical fracture running through it. The sample cut from the rock slab was $200 \times 200 \times 250 \text{ mm}^3$ containing the partially mated fracture. A force of approximately 100 Nm was required to break the remaining rock bridges between the surfaces and open the fracture (Bruines, 2022). Figure 1a shows the fracture surface after opening.



Figure 1. Upper surface of the fracture after opening (a), 3D scan of the surface (b) and surface after interpolation from point cloud data to a regular grid (c).

Once opened, the upper and lower surface were scanned using a handheld laser scanner (Figure 1b). The surface scan data required pre-processing before it could be used to obtain the parameters needed for aperture generation (Stock & Frampton, 2022). The scanning method used results in an irregular mesh. This means on the XY coordinate plane, the nodes on the upper and lower surface will not align. Due to this, the surface data is linearly interpolated onto a regular grid with a resolution of 0.1 mm in order to easily obtain the aperture field (Figure 1c). Areas near the edge of the scan tend to contain errors so the edges are cropped to remove obviously erroneous data. Issues arise from vertical referencing of the upper and lower surface scans, resulting in an unrealistic aperture field with many negative aperture values. To correct this the lower surface is translated relative to the upper surface to improve alignment and reduce inaccurate negative apertures. However, this is insufficient to fully correct the aperture field, so pressure film data that was also provided was used as a reference to vertically shift the upper surface until a visual best fit aperture field distribution is achieved. Further details on pre-processing the surface scan data are presented by Stock and Frampton (2022).

After pre-processing, the surface scans produce an aperture that contains a few abnormal isolated larger apertures, which are most likely due to rock fall out during opening of the fracture. Figure 2 shows the rock fall out collected after opening (a) and the aperture when 5% of the largest apertures have been removed (b). As can be seen, the largest values generally occur in isolated locations across the aperture field. Areas that have a constant value of zero are considered contact points, and areas that are white are where data has been removed (b). An interpretation of the pressure film is also shown (c) with locations of the rock fall out highlighted, white areas represent void spaces that are larger than the thickness of the pressure film ($200 \mu\text{m}$) and red represents a pressure of 50 MPa.

Figure 3 shows the normalised cumulative distribution and box plots for the same aperture whilst systematically filtering the largest values from the data by area. Zero percent represents the full aperture with no data removed and 5% represents the aperture where the largest 5% of aperture values are removed. During opening the fracture, release of stress could lead to the surface level increasing, which results in a negative aper-

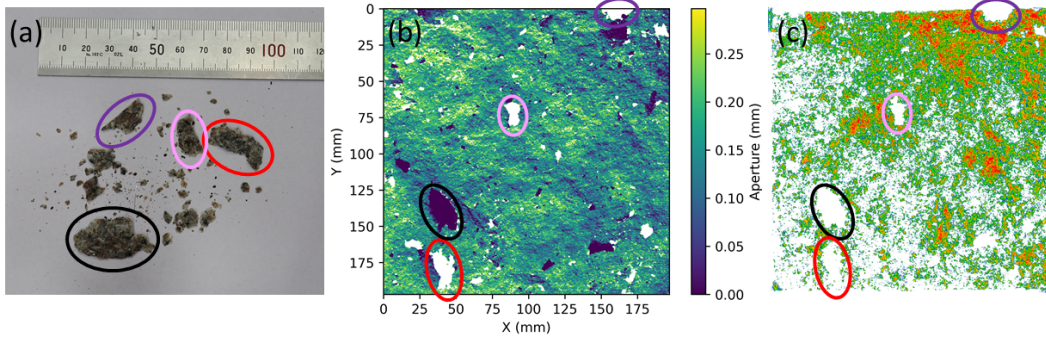


Figure 2. Rock fall out collected after opening the fracture (a) with the possible locations of fall out located on the aperture field by red, black and pink circles (b) and pressure film data (c)

297 ture when the lower surface is subtracted from the upper surface. Therefore, all nega-
 298 tive apertures have been set as zero and are assumed to be contact areas. Removing the
 299 largest 1% of apertures significantly reduces the maximum aperture by approximately
 300 2 mm, this highlights how isolated the largest apertures are. As increasingly larger per-
 301 centages of the aperture are removed, the maximum values decrease whilst only having
 302 small changes on the aperture distribution. The change in distribution is mainly observed
 303 as the normalised cumulative distribution reaches approximately 0.9, and apertures with
 304 a higher percentage of filtering reach the peak sooner. The differences between succes-
 305 sive percentage increase of filtering become smaller, with 4% and 5% having only minor
 306 differences in distribution. Box plots for the distributions (Figure 3b) show a decrease
 307 in most values as larger percentages of the aperture are removed. However, the median
 308 value remains fairly constant, decreasing from 0.149 mm at 0% to 0.146 mm at 5% fil-
 309 tering. The consistency in the medians shows that when the whole aperture is consid-
 310 ered the largest apertures are outliers within the data set. No outliers are present at 5%
 311 filtered, so this aperture is used for comparison with the generated aperture.

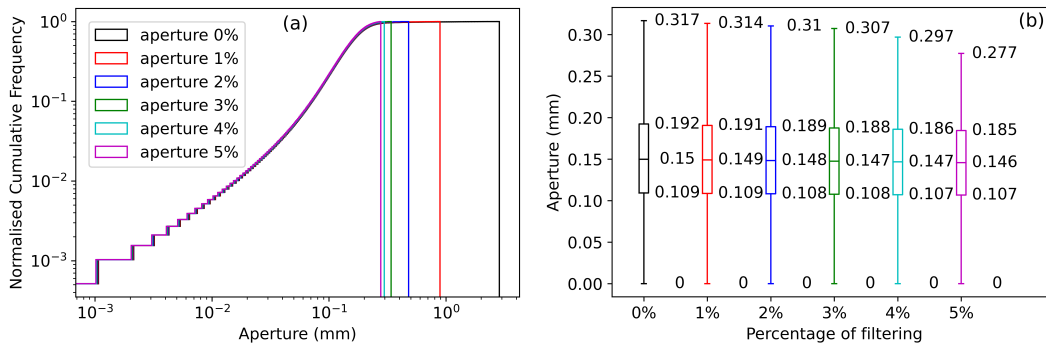


Figure 3. Normalised cumulative distributions of the measured aperture with the maximum apertures filtered by increasing percentages of area (a) and corresponding box plots (b)

312 2.4 Fracture surface and aperture generation

313 Several trace profiles are taken across each of the two fracture surfaces (cf. upper,
 314 shown in Figure 1c) in the X and Y directions along every mesh cell, so that the total
 315 number of profiles in one direction is the same as the total number of cells along one edge

length. This results in 1970 trace profiles in each direction, with a length resolution of each trace profile of 0.1 mm. The RMS-COR method is then executed on every profile, providing a Hurst and scaling parameter for each profile, where a combination of parameters that most closely represents the surface must be selected (section 3.1). Relative anisotropy is calculated by using the median of the ratios $H(X)/H(Y)$. The Hurst exponent and anisotropy are then used to define the amplitude of the Fourier components.

When all the Fourier components are known and arranged in a 2D complex and symmetric matrix in the correct position regarding wavenumber, a 2D Fast Fourier Transformation is executed over the data, the real part of which represents the fracture surface with a mean value of zero. The last steps are to scale the surface to the required size, and scale the asperities to that defined by the scaling parameter obtained from the RMS-COR method, and vertically shift the mean level of the fracture surface such that no negative values occur in the aperture field. It is important to account for different trace resolution between the real data and generated aperture, so the scaling value can be corrected to represent the same resolution, and hence produce an accurate re-scaling of the surface and aperture. Note that the topography of each pair of surfaces will depend on the random number sequence used to select the correlation arrays. Therefore, due to this stochastic nature of sampling, an ensemble of fracture aperture realisations must be generated for a given set of input parameters in order to obtain a sufficiently large sample size to compare against the measured fracture aperture. However, we stress that each generated sample is an equally probably realisation based on a given set of input values. Therefore, this can enable a convenient approach for generating multiple fractures based on a limited number of fracture measurements. Furthermore, since the scaling behaviour of the surface and relative positions of different size asperities is controlled by the Hurst exponent, it enables a convenient approach to up-scaling fracture surfaces, based on the assumption of the properties of the rough surfaces being self-affine for the spatial scales considered and the correlation between surfaces being scale independent.

3 Results

3.1 Fracture surface and aperture field

The PSDR obtained from the fracture with a third order polynomial regression plotted over the PSDR is shown in Figure 4a. The variation in correlation with wavenumber shows the decrease in correlation (Figure 4b, red line) as wavenumber increases. The number of wavenumbers over which the correlation is applied has been re-scaled to correspond with the dimensions at which the aperture realisations will be generated at. As can be seen, the correlation 1 - PSDR (Figure 4b, blue line) initially decreases before increasing again at approximately 50, however the correlation reaches a minimum value of approximately 0.86. The increase thereafter is an artefact due to the resolution of the surface scans and the resolution at which the surfaces were interpolated on to a regular grid. If one value in the point cloud is interpolated over more than one grid cell then 1 - PSDR will increase. This artifact is removed from the correlation array (red line) by manually setting the minimum value for increasing wavenumbers. This adjusted correlation function is then used in the subsequent number swapping algorithm.

The RMS-COR method is then executed on trace profiles across both surfaces in the X and Y directions every 0.1 mm using a maximum step length of 10% (Δv , Eq 3), resulting in 1,970 values of both Hurst exponent and scaling parameter in each direction on the upper and lower surfaces. The 75th percentile for Hurst exponent and scaling parameter have been used to generate the partially correlated upper and lower surfaces and resulting aperture field that are seen in Figure 5. The cumulative density function of the single realisation of the aperture field is shown in Figure 6a. Thereafter, multiple realisations using the same input parameters are generated; the ensemble of 100 realisations are shown in Figure 6b.

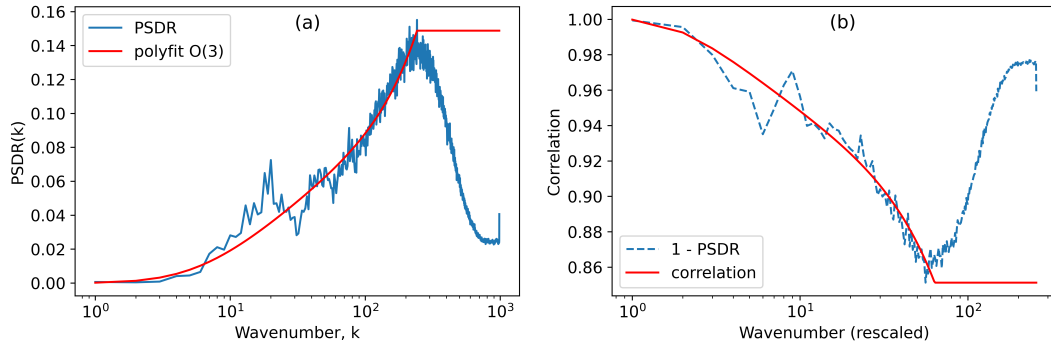


Figure 4. PSDR with a third order polynomial regression (a) and change in correlation with rescaled wavenumbers (b)

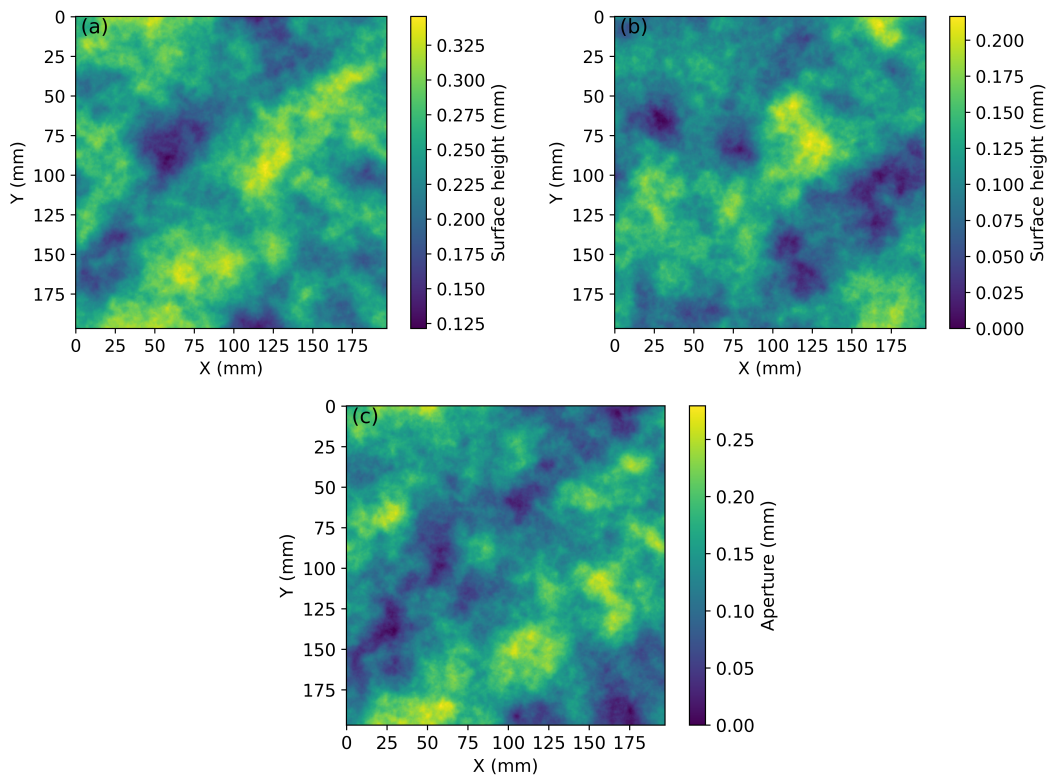


Figure 5. Generated upper surface (a), lower surface (b) and resulting aperture field created from the semi correlated surfaces (c)

367 The spread in aperture distribution is due to the stochastic nature of the method,
 368 therefore multiple realisations are required to be generated until the aperture ensemble
 369 stabilises. The number of realisations required is evaluated by using the two-sided Kolmogorov-
 370 Smirnov test to compare the measured aperture distribution with increasing generated
 371 aperture ensembles (Table 1). A smaller KS value represents a closer match, and a value
 372 of 0 indicates the two empirical distributions are identical. This shows that 50 realisa-
 373 tions and greater will show very little variation; in the main analysis 100 realisations are
 374 used.

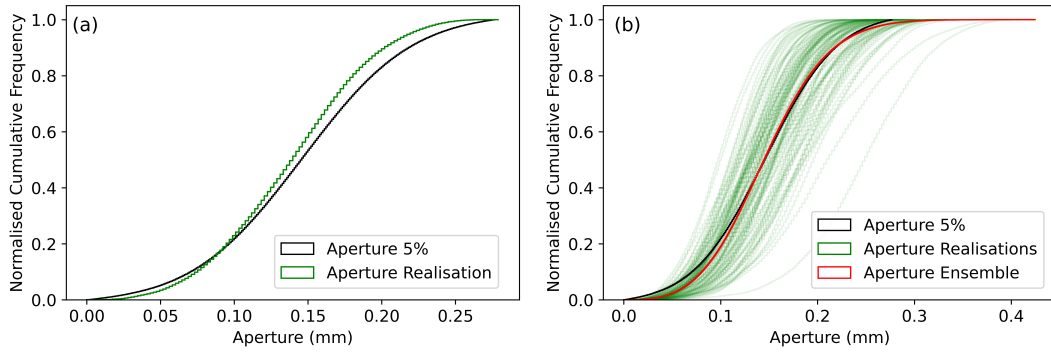


Figure 6. Cumulative distribution of one realisation (a) and a 100 realisations with generated aperture ensemble (b)

Table 1. KS test statistic for ensembles comprised of increasing number of aperture realisations tested against the 5% filtered measured aperture

No. of realisations	KS statistic
10	0.043
20	0.056
50	0.035
100	0.034

375 There is a significant spread in Hurst and scaling parameters, and which differs slightly
 376 between the upper and lower surfaces (Figure 7a,b). The Hurst exponent ranges from
 377 approximately 0.6 to 1 for both the upper and lower surface but a larger difference be-
 378 tween the surfaces is seen in the scaling parameter, which ranges from 0.025 to 0.06 and
 379 0.025 to 0.07 for the upper and lower surfaces respectively. The 25th, median and 75th
 380 percentiles have been calculated for both Hurst exponent and scaling parameter (Table
 381 2). The input parameters from the 75th percentiles generate an aperture ensemble dis-
 382 tribution that corresponds well with the measured aperture field scans, better than us-
 383 ing the median, and the 25th percentile showing the most dissimilar distribution (Fig-
 384 ure 7c). However, note that any of the parameter combinations plotted could be used
 385 for aperture generation, so the combination that produces an ensemble most similar to
 386 the aperture data must be determined.

387 3.2 Parameter sensitivity analysis

388 The analysis of the fracture scans yields a wide range of values for the Hurst ex-
 389 ponent and scaling parameter (Figure 7 and Table 2). Here we present an analysis of these
 390 parameter combinations in terms of their impact on the resulting generated aperture field
 391 distribution. A regular grid of points across the parameter space is considered, which
 392 has the advantage of providing a systematic analysis for regions both covered by the pair-
 393 wise correlated Hurst and scaling parameters as well as regions beyond. Each pair of Hurst
 394 exponent and scaling parameter in the grid is used to generate 100 realisations of the
 395 aperture field, and the ensemble evaluated against the measured aperture distribution.
 396 The similarity of the generated ensembles with the measured aperture was assessed us-
 397 ing the Kolmogorov–Smirnov (KS) test statistic, which measures the largest difference
 398 between the distributions of the two samples. Figure 8 shows an overlay of the KS statis-
 399 tic value, where a smaller value means a better fit between the distributions, on the reg-

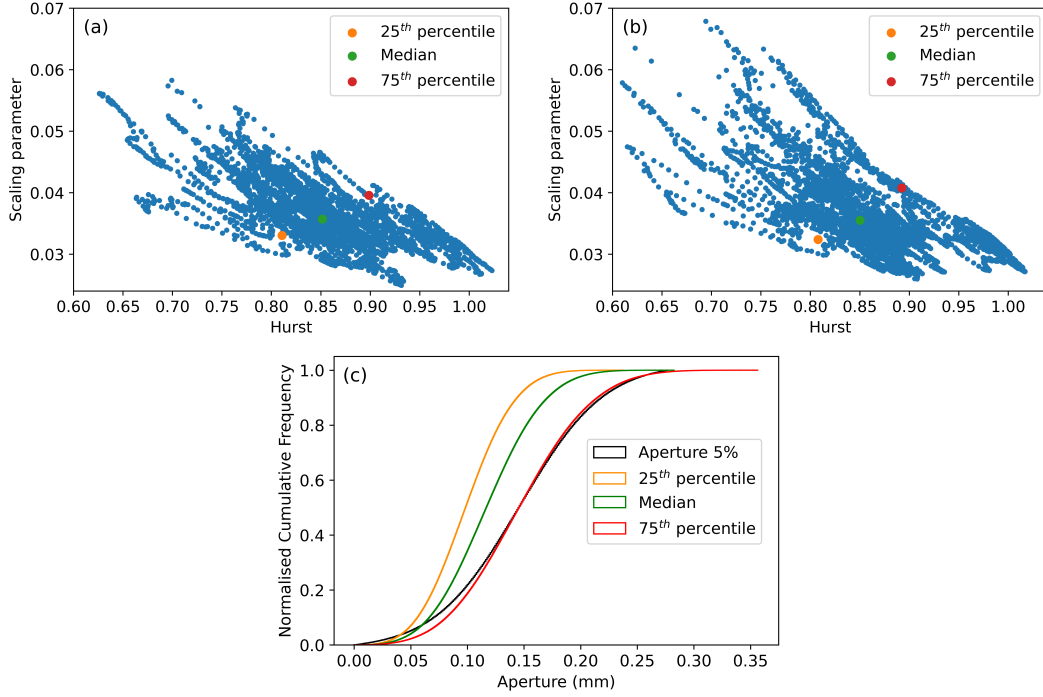


Figure 7. Hurst exponent and scaling parameter from each trace profiles along X and Y directions for the upper (a) and lower (b) surfaces and the corresponding cumulative distribution of the aperture ensembles using the 25th, median and 75th percentiles as input parameters (c)

Table 2. The 25th, median and 75th percentiles for Hurst exponent and scaling parameters for the upper and lower surfaces using different maximum step lengths in the RMS-COR function

Upper surface	Step length 20%		Step length 10%		Step length 5%	
	Hurst	Scaling	Hurst	Scaling	Hurst	Scaling
25 th percentile	0.660	0.040	0.811	0.033	0.875	0.030
Median	0.755	0.046	0.851	0.036	0.913	0.032
75 th percentile	0.822	0.057	0.899	0.040	0.947	0.034
Lower surface	Step length 20%		Step length 10%		Step length 5%	
	Hurst	Scaling	Hurst	Scaling	Hurst	Scaling
25 th percentile	0.653	0.040	0.808	0.032	0.873	0.029
Median	0.747	0.047	0.850	0.036	0.913	0.031
75 th percentile	0.817	0.057	0.892	0.041	0.951	0.035

400 ular grid parameter points over the scatter plots of parameters on the upper and lower
 401 surfaces. A linear regression was plotted using the weighted overlay to follow the trend
 402 of best fits (Figure 8, black line) which generally follows the upper bound of the param-
 403 eters. Moving away from this trend results in an increase in the KS statistic value as the

404 parameter combinations generate apertures that are less similar to the measured aper-
 405 ture. The 75th percentile combination for the Hurst and scaling parameter is very close
 406 to the linear regression line, and the ensemble generated using these values has the small-
 407 est KS statistic value. Therefore these values are used as input parameters for the final
 408 aperture generations.

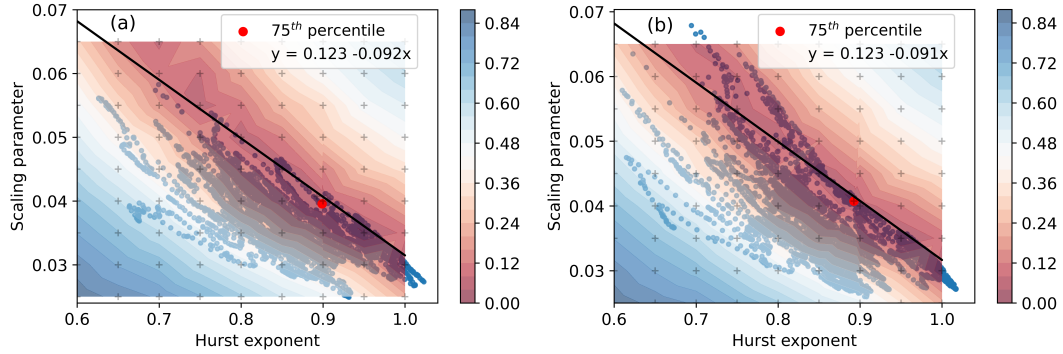


Figure 8. Hurst exponent and scaling parameter scatter plot overlain with fitting metric results for the upper (a) and lower (b) surfaces with the 75th percentile highlighted and regression line plotted using the weighted overlay

409 Figure 9a shows the correlation obtained from a polynomial fit which we propose
 410 here (red line) compared against the correlation obtained using the approach suggested
 411 by Ogilvie et al. (2006) (blue line). It can be seen that our approach has a lower gra-
 412 dient of change from low to high correlation, meaning that at larger wavelengths the sur-
 413 faces are not as strongly correlated as they would be compared to the approach by Ogilvie
 414 et al. (2006). The main difference is that the approach we suggest uses all of the infor-
 415 mation obtained from the PSDR analysis of the fracture scan sample; it does not solely
 416 rely on end points of the correlation and length over which the transition occurs. By in-
 417 troducing the polynomial fit of the PSDR, the generated aperture ensemble distribution
 418 is improved and better corresponds with the measured fracture sample (Figure 9b).

419 Box plots for the filtered aperture show the aperture ensemble generated using the
 420 Ogilvie et al. (2006) method and the new model developed in this paper (Figure 9c). This
 421 shows that the Ogilvie et al. (2006) method under predicts the distribution, with each
 422 of the values being lower than the filtered aperture data. However, the new model has
 423 a distribution that is very similar; the median value is only 0.001 mm smaller, with the
 424 biggest difference seen in the upper whiskers which are 0.013 mm larger.

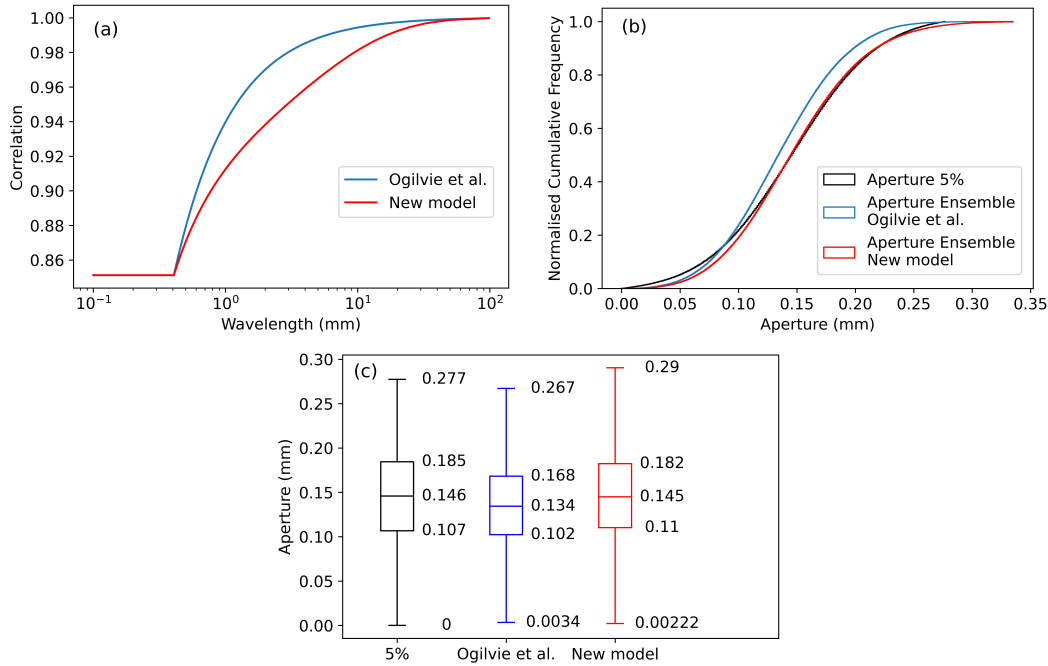


Figure 9. Comparison of Ogilvie method and the new model correlation with wavelength (a), aperture ensemble distribution generated from the new correlation and input parameters (b) and box plots of the 5% filtered aperture, Ogilvie method and new model ensemble (c)

4 Discussion

4.1 Field data filtering

During opening of the fracture some rock was broken off (Figure 2a), and although the volume of this debris is unknown it could be the cause of isolated and abnormally large apertures seen in the unfiltered distribution (cf. Figure 3a). The shape of some of the debris has similar geometry to the larger apertures, which further suggests that rock fall out is the cause. This is highlighted by red, black, purple and pink circles around rock debris and the possible location on the aperture field. The red, purple and pink circle encompass rock pieces that have a distinct shape, which seems to also be present in the aperture field and also in the pressure film data (Figure 2b,c). If the rock debris would have remained intact in these locations, the corresponding apertures would be significantly smaller. However, it is difficult to predict how adding the rock pieces would affect the apertures. For this reason, the aperture data has been filtered to remove the largest 5% of apertures, which should correct for the rock fallout and provide a more accurate representation of the distribution of the aperture when it was unopened. However, excessive filtering increases the risk of unintentional removal of large natural fracture apertures. We determined the threshold limit of 5% to be a reasonable balance without excessively impacting the overall shape of the aperture distribution (cf. Figure 3).

Another piece of rock fallout that visually fits well is highlighted by a black circle. This location represents a contact area, which is due to the subtraction of the lower surface scan from the upper resulting in a negative aperture, hence it is corrected to zero. It is not intuitive how additional rock mass would correct this, however from the pressure film data there is also a large void space at this location. This suggests that the rock piece was loosely attached during scanning, but has fallen off before the pressure film measurements were taken. If the piece was attached then a higher pressure would be ex-

450 pected, representing close contact, however it can be seen there is a void space at this
 451 location (Figure 2, black circle). This highlights further that great care should be taken
 452 when using the pressure film to vertically align the surfaces, as the 3D scan data and pres-
 453 sure film may not represent exactly the same state of the surfaces and resulting aper-
 454 ture field.

455 4.2 Hurst exponent and scaling parameter space

456 The spread of Hurst exponent and scaling parameter is in part due to the maxi-
 457 mum step length that is used when calculating RMS-COR function. Figure 10a,b shows
 458 the spread of parameters using a step length of 20%, 10% and 5% (orange, blue and green
 459 respectively) of the maximum trace length. Reducing the step length reduces the like-
 460 lihood of the regression line curving in log-log space, and hence reduces the spread (Marsch
 461 & Fernandez-Steeger, 2021). It should be noted that changing the step length has no ef-
 462 fect on the total number of Hurst and scaling values as the same number of trace pro-
 463 files are used. When a maximum step length of 20% is used the spread is large, rang-
 464 ing from approximately 0.35 to over 1 for the Hurst exponent. Small Hurst exponents
 465 seen in this range are not likely to be seen on fracture surfaces, as generally the Hurst
 466 exponent will range from 0.5 to 1 (S. Brown, 1987). As Hurst exponent decreases, it can
 467 be seen that some values of scaling parameter and Hurst exponent create a trend away
 468 from the main bulk of the scatter plot. This can most clearly be seen for a maximum
 469 step length of 20% at the lower Hurst exponent values. Potentially this could be due to
 470 trace profiles that go over sections where substantial parts of rock surface have fallen out
 471 during opening, which may perturb the assumption of the fractal nature of the fractures.
 472 Reducing the step lengths reduces the spread of these data away from the main bulk of
 473 the scatter plot, reducing errors that have been introduced from a larger step length. This
 474 reduction also decreases the extent by which the scatter plot data goes above the lin-
 475 ear regression that represents a line along which parameter combinations produce the
 476 best correspondence between aperture ensemble distributions and the measured aper-
 477 ture.

478 For the upper surface it is only the data obtained from a maximum step length of
 479 20% that has a significant amount of values above the regression line, with the other two
 480 data sets mostly staying below this line. This shows that for the upper surface the best
 481 parameter combinations fall on the upper bound of the data. For the lower surface this
 482 is not so obvious, as regardless of the step length, some of the parameter combinations
 483 fall above the linear regression. The Hurst exponent at which the values go above the
 484 linear regression decreases as the maximum step length increases. However for smaller
 485 step lengths, the majority of the data points stay below the linear regression line, sug-
 486 gesting the influence of rock fall out is also present in the lower surface. Table 2 shows
 487 the affect of maximum trace length on the 25th, median and 75th percentiles for Hurst
 488 exponent and scaling parameter.

489 When the maximum step length of 10% is used, the 75th percentile is on the up-
 490 per bound of the data for both the upper and lower surface, which also is very close to
 491 the regression line that represents the parameter combinations that produce the best aper-
 492 ture ensembles (Figure 10c,d). When the step length is reduced further to 5% then 75th
 493 percentile is slightly further away, but would still produce reasonably good aperture en-
 494 sembles. However, if a larger maximum step length is used then this value moves sig-
 495 nificantly above the regression line, which is seen for the maximum step length of 20%
 496 and would not produce an aperture ensemble that corresponds well with the measured
 497 aperture. This shows that a maximum step length of 10% is best when the full surface
 498 is used to obtain the 75th percentile parameter combination. This percentile lies on the
 499 upper bound of the data and is easy to calculate, making it easy to find this parame-
 500 ter combination as the input. However, any parameter combination along the linear re-
 501 gression line could be used as the input and produce an aperture ensemble that corre-

502 sponds with the measured aperture. The surfaces will have different topographies, but
 503 the resulting aperture distributions will be consistent. The regression line could represent
 504 a natural upper limit of the surface roughness, where values along this line best represent
 505 that specific surface. Hence, different rock and fracture types with different properties
 506 may have a different gradient to the line of regression.

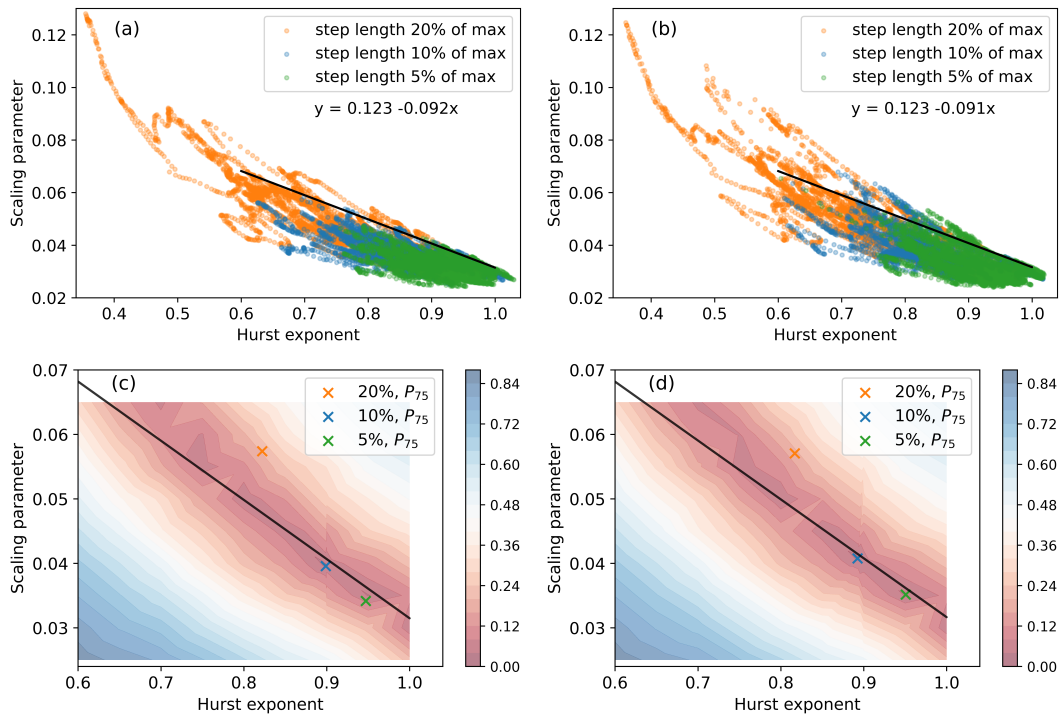


Figure 10. Upper (a) and lower (b) surface Hurst and scaling parameters for 20%, 10% and 5% of the maximum step length and regression line calculated from best fit overlay. The 75th percentiles for a maximum step length of 20%, 10% and 5% for the upper (c) and lower (d) surfaces and the linear regression line following the best fits

507 The method used to calculate Hurst exponent and scaling parameters used in this
 508 study is different from Ogilvie et al. (2006) as they used the slope of power spectral density
 509 to obtain these parameters. However, using the power spectral density to obtain input
 510 parameters can be affected more greatly by rock fall out which creates areas that
 511 are no longer self-affine. When used to calculate the Hurst exponent from these surfaces
 512 the result is a value of 0.52, compared to approximately 0.9 which is the 75th percentile
 513 value of the method we use. This could have worked for Ogilvie et al. (2006) as the frac-
 514 tures used in that study were artificially induced, therefore there was not the issue of forc-
 515 ing the fracture open and damaging the surfaces in the process to produce rock fall out.
 516 Since the fracture in this study is natural, using many traces across the surface and the
 517 RMS-COR evaluation method works better. This also allows the values which are most
 518 representative of the surface to be selected, as well as allowing the scaling parameter to
 519 be obtained from the same method.

520 This method can also work on fracture trace profiles, if the full surface is not avail-
 521 able for analysis. The correlation can be obtained from this data, but only one set of par-
 522 ameter combinations will be obtained, meaning the 75th percentile is unknown. In this
 523 case a maximum step length of 5% is best, as the spread of data is reduced (Figure 10a,b),

524 so it more likely that the Hurst and scaling parameter will be close to the best fit regres-
 525 sion line.

526 4.3 Upper and lower surface correlation

527 The model for aperture generation presented in this work has updated the method
 528 in which the correlation with scale changes. The PSDR is used, as it is in Ogilvie et al.
 529 (2006), but each wavenumber is used, which avoids the need to calculate a linear change
 530 between minimum and maximum correlation between the surfaces. Instead we can plot
 531 a polynomial regression through the PSDR (Figure 4) and base the correlation for each
 532 wavenumber off this, giving a more realistic transition from low to high correlation be-
 533 tween the surfaces as the scale changes. Depending on the order of polynomial however,
 534 it might not capture all the fluctuations. For example, as the correlation decreases with
 535 increasing wavenumber (decreasing scale) there are small fluctuations around wavenum-
 536 ber 9 (Figure 4). The fluctuations could be a result of large isolated apertures, as this
 537 wavenumber is approximately equivalent to the distance between large apertures, and
 538 could lead to the spike in the power spectral density that is observed. This fluctuation
 539 is not however captured in the correlation if a low order polynomial is used.

540 A sensitivity analysis of the aperture generation model to correlation with scale was
 541 tested using several different order polynomial regression fits. As can be seen from Fig-
 542 ure 11a,b using order 3, 9 and 16 has very little effect on the overall distribution. This
 543 suggests that it is the general trend that is more important to capture than every small
 544 fluctuation. The general trend captured from a third order polynomial regression is dif-
 545 ferent from the linear change that has been implemented in previous methods, and the
 546 improvements can be seen in Figure 9 where the update to correlation produces a gener-
 547 ated aperture ensemble distribution that highly corresponds with the measured aper-
 548 ture field.

549 Also, a synthetic analysis was conducted over an arbitrarily selected correlation with
 550 scale, but one that could be expected within reality (Figure 11c). Ten cases, each with
 551 a 100 fracture aperture realisations were systematically generated, with initially only wavenum-
 552 ber 1 correlated to the maximum value, increasing until the first 10 wavenumbers have
 553 a constant high correlation. After this point there is a decrease in correlation as the wavenum-
 554 bers increase as would be expected in a natural fracture. Distributions created with wavenum-
 555 bers 2 to 10 highly correlated are grouped together, and show no systematic change as
 556 the wavenumbers increase (Figure 11d). However when only wavenumber 1 is highly cor-
 557 related, it is clearly separate from the other distributions. This suggests that correlat-
 558 ing the first wavenumber correctly is more important than the following wavenumbers
 559 as the scale increases. Using a low order polynomial regression allows the first wavenum-
 560 ber to be accurately obtained while plotting the general trend of correlation for the fol-
 561 lowing wavenumbers, allowing an accurate representation of the aperture field to be pro-
 562 duced.

563 Although the large apertures have been filtered out when comparing the realisa-
 564 tions to the measured aperture, they are still present when calculating the PSDR and
 565 the correlation with scale. This may lead to slightly inaccurate correlation within the
 566 generated apertures. This could be corrected for if a reliable method for correcting sur-
 567 face scans is produced. However, currently there is no way to accurately digitally replace
 568 any rock fall out. To remove these areas during the matching analysis would also pro-
 569 duce errors with the correlation, most likely to an even greater extent. Errors from the
 570 matching analysis are a direct consequence of fall out during opening the fracture and
 571 scanning. Therefore it is imperative that this process be done as accurately as possible
 572 to allow for more accurate realisations of the aperture to be generated.

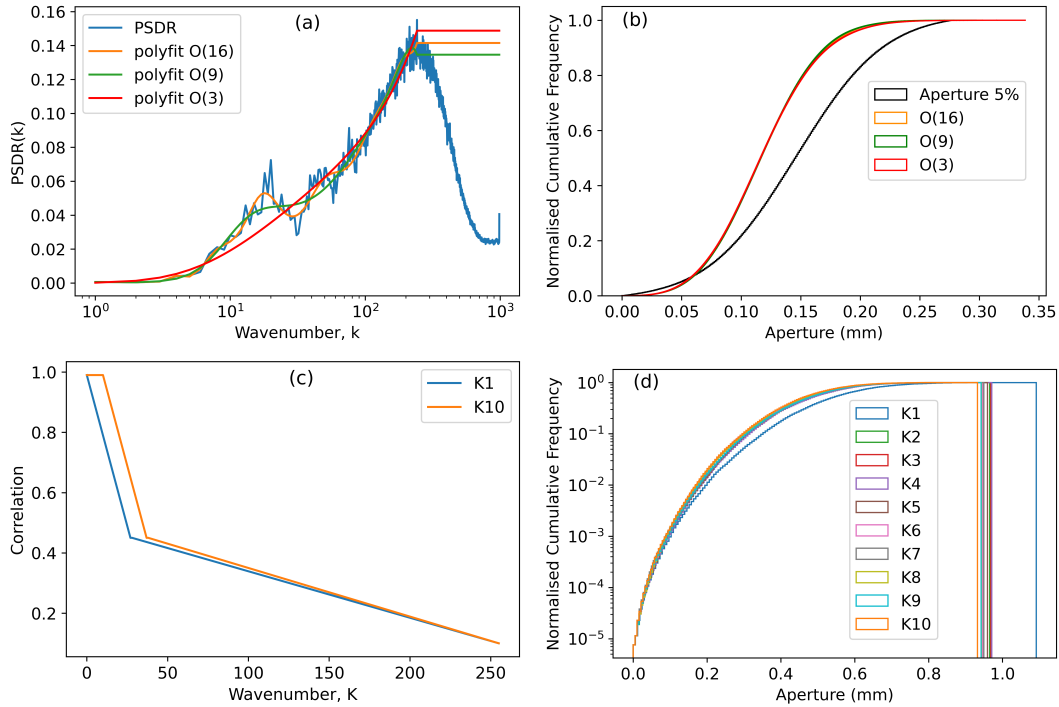


Figure 11. PSDR with different orders polynomial regression fits (a) and the resulting aperture distribution ensembles (b). Change in correlation with wavenumber for cases with the first wavenumber, K1, and the first 10 wavenumbers, K10, highly correlated (c) and the effects of increasing the amount of wavenumbers (K) that have the highest correlation on the aperture ensemble (d)

573

4.4 Implications for up-scaling

574

575

576

577

578

579

580

581

582

583

584

585

586

587

588

589

590

591

592

593

One reason for developing this method is to allow for representations of real fracture apertures to be up-scaled and implemented within larger scale DFNs. Figure 12a,b shows a scatter plot of Hurst exponent and scaling parameter for the full surface and a 100 mm^2 subsection. The linear regression represents the line along which the parameter combinations show the best correspondence with the measured aperture. As can be seen the 75th percentiles are situated close to the linear regression for parameters obtained from both sized sections, where blue represents the subsection and orange represents the full surface. For up-scaling the Hurst and scaling parameter should be selected from the upper bound of the data, and not a single value. The cropped section of the full surfaces has been used to generate an ensemble of 100 aperture realisations which have been up-scaled to $197 \times 197 \text{ mm}^2$, the results of which can be seen in Figure 12c,d. The difference between the median is 0.01 mm for the full aperture and 0.006 mm for the cropped aperture field. When the matching analysis is undertaken on the subsection, the correlation between the surfaces is slightly weaker, resulting in larger apertures when the up-scaled apertures are generated, leading to the difference in medians. However, overall the difference is only small and the ensemble corresponds moderately well with the measured aperture data, showing that this method can be used to up-scale aperture fields to any desired dimensions. Although this method does allow for up-scaling based solely on a fracture trace profile, it will not be as accurate as using a surface scan of the fracture surfaces.

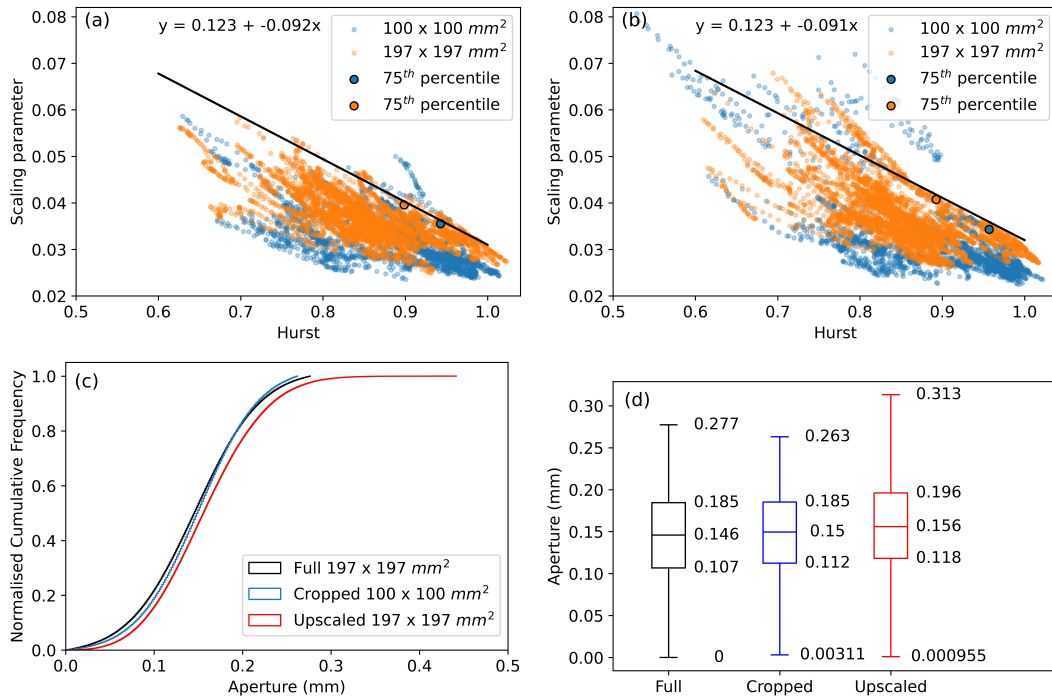


Figure 12. Hurst exponent and scaling parameter for the upper (a) and lower (b) surfaces with different dimensions, cumulative frequency of the full aperture, cropped and up-scaled aperture ensemble (c) and resulting box plots (d).

5 Conclusion

The method developed in this study can generate apertures that are representative of natural rock fractures based on data from high resolution 3D fracture surface scans. During opening of the fracture, rock debris fell out, resulting in abnormally large apertures in the measured aperture distribution, which required filtering before comparison. The generated aperture ensemble distribution shows very high correspondence with the filtered measured aperture distribution. The approach to obtaining a correlation between upper and lower fracture surfaces has been improved based on previous methods by using a third order polynomial regression. This results in a general trend of change in correlation with scale which is implemented over the required wavenumbers. The changes in the minimum correlation at high wavenumbers can slightly affect the aperture distribution which can be seen from the up-scaled aperture realisations.

However it was found that fluctuations in correlation between the surfaces is not as sensitive as the input parameters that are used. The Hurst and scaling parameter are shown to exhibit a clear linear correlation, visible when plotted on a scatter plot; as the Hurst exponent increases the scaling parameter decreases. Reducing the maximum step length in the analysis of profile traces along the fracture surfaces reduces the spread of data and the number of outliers deviating away from the main trend.

Also, we show that using the 75th percentiles for the Hurst exponent and the scaling parameter result in aperture distributions that correspond very well with the measured data. It was found that any parameter combination along a linear regression which follows the upper bound of correlation between the Hurst and scaling parameters would result in an aperture ensemble with high correspondence with the measured data. It is suggested that this upper bound could represent a natural upper limit for this rock or

618 fracture type, and the gradient of this trend may change depending on different rock types
 619 and stress state under which the fracture was induced. This method does not solely rely
 620 on full surface scans and can be readily used on surface profiles, in which case, the pa-
 621 rameter inputs should be obtained preferably with a relatively short maximum step length
 622 of 5%.

623 The way in which the surfaces are generated and the correlation between them, up-
 624 scaling of the generated apertures can be easily achieved. When the 75th percentiles for
 625 Hurst exponent and scaling parameter are calculated for a subsection of the full surfaces,
 626 the values are close to the linear regression calculated for the full surface. These values
 627 and the correlation between upper and lower surfaces of the subsection were successfully
 628 used to generate up-scaled aperture fields representing the full surface with moderately
 629 high correspondence. Aperture fields generated using this method are representative of
 630 natural fracture apertures and could be used for modelling larger fractures or multiple
 631 fractures, allowing for large scale discrete fracture network simulations to include realis-
 632 tic representation of aperture internal heterogeneity.

633 6 Data availability statement

634 The fracture surface data used for supporting the results presented in this paper
 635 are openly available from <https://doi.org/10.5281/zenodo.8354914> (Stock, 2023).

636 Acknowledgments

637 B. S. and A. F. gratefully acknowledge funding from the Swedish Nuclear Fuel and Waste
 638 Management Co. (SKB) and the Rock Engineering Research Foundation (BeFo).

639 References

- 640 Brown, S. (1987). Fluid flow through rock joints: The effect of surface rough-
 641 ness. *Journal of Geophysical Research: Solid Earth*. Retrieved 2020-08-31,
 642 from [https://agupubs.onlinelibrary.wiley.com/doi/abs/10.1029/
 643 JB092iB02p01337?casa_token=tRmMqdF21RoAAAAA:xztBT0RA4hXEgMe_Vx
 644 _z94i2XHXTsnCbhKnfCwChe1n7BV5zMsvcTCQN82UPQCLQTBavAW4mfiiuu6DU](https://agupubs.onlinelibrary.wiley.com/doi/abs/10.1029/JB092iB02p01337?casa_token=tRmMqdF21RoAAAAA:xztBT0RA4hXEgMe_Vx_z94i2XHXTsnCbhKnfCwChe1n7BV5zMsvcTCQN82UPQCLQTBavAW4mfiiuu6DU)
- 645 Brown, S. R. (1995a). Measuring the Dimension of Self-Affine Fractals: Example
 646 of Rough Surfaces. In C. C. Barton & P. R. La Pointe (Eds.), *Fractals in the
 647 Earth Sciences* (pp. 77–87). Boston, MA: Springer US. Retrieved 2022-11-
 648 10, from https://doi.org/10.1007/978-1-4899-1397-5_4 doi: 10.1007/978
 649 -1-4899-1397-5_4
- 650 Brown, S. R. (1995b). Simple mathematical model of a rough fracture. *Journal of
 651 Geophysical Research: Solid Earth*, 100(B4), 5941–5952. Retrieved 2021-10-
 652 05, from <https://onlinelibrary.wiley.com/doi/abs/10.1029/94JB03262>
 653 (_eprint: <https://onlinelibrary.wiley.com/doi/pdf/10.1029/94JB03262>) doi:
 654 10.1029/94JB03262
- 655 Brown, S. R. (1998). *Experimental observation of fluid flow channels in a
 656 single fracture - Brown - 1998 - Journal of Geophysical Research: Solid
 657 Earth - Wiley Online Library*. Retrieved 2020-08-31, from [https://
 658 agupubs.onlinelibrary.wiley.com/doi/abs/10.1029/97JB03542](https://agupubs.onlinelibrary.wiley.com/doi/abs/10.1029/97JB03542)
- 659 Brown, S. R., & Scholz, C. H. (1985). Closure of random elastic surfaces
 660 in contact. *Journal of Geophysical Research: Solid Earth*, 90(B7),
 661 5531–5545. Retrieved 2022-05-24, from [https://onlinelibrary
 662 .wiley.com/doi/abs/10.1029/JB090iB07p05531](https://onlinelibrary.wiley.com/doi/abs/10.1029/JB090iB07p05531) (_eprint:
 663 <https://onlinelibrary.wiley.com/doi/pdf/10.1029/JB090iB07p05531>) doi:
 664 10.1029/JB090iB07p05531
- 665 Bruines, P. (2022). *Description of Task 10.2 - Channelling in a single fracture*.

- 666 *Task 10 of SKB Task Force GWFTS - Validation approaches for groundwa-*
 667 *ter flow and transport modelling with discrete features. SKB P-22-06, Svensk*
 668 *Kärnbränslehantering AB.*
- 669 Cacas, M. C., Ledoux, E., Marsily, G. d., Tillie, B., Barbreau, A., Durand, E., ...
 670 Peaudecerf, P. (1990). Modeling fracture flow with a stochastic discrete frac-
 671 ture network: calibration and validation: 1. The flow model. *Water Resources*
 672 *Research*, 26(3), 479–489. Retrieved 2020-09-17, from [https://agupubs](https://agupubs.onlinelibrary.wiley.com/doi/abs/10.1029/WR026i003p00479)
 673 [.onlinelibrary.wiley.com/doi/abs/10.1029/WR026i003p00479](https://agupubs.onlinelibrary.wiley.com/doi/abs/10.1029/WR026i003p00479) (_eprint:
 674 <https://agupubs.onlinelibrary.wiley.com/doi/pdf/10.1029/WR026i003p00479>)
 675 doi: 10.1029/WR026i003p00479
- 676 Candela, T., Renard, F., Bouchon, M., Brouste, A., Marsan, D., Schmittbuhl, J., &
 677 Voisin, C. (2009, October). Characterization of Fault Roughness at Various
 678 Scales: Implications of Three-Dimensional High Resolution Topography Mea-
 679 surements. *Pure and Applied Geophysics*, 166(10-11), 1817–1851. Retrieved
 680 2021-06-02, from <http://link.springer.com/10.1007/s00024-009-0521-2>
 681 doi: 10.1007/s00024-009-0521-2
- 682 Durham, W. B., & Bonner, B. P. (1994). Self-propping and fluid flow in
 683 slightly offset joints at high effective pressures. *Journal of Geophysical*
 684 *Research: Solid Earth*, 99(B5), 9391–9399. Retrieved 2020-04-24, from
 685 <https://agupubs.onlinelibrary.wiley.com/doi/abs/10.1029/94JB00242>
 686 (_eprint: <https://agupubs.onlinelibrary.wiley.com/doi/pdf/10.1029/94JB00242>)
 687 doi: 10.1029/94JB00242
- 688 Frampton, A., & Cvetkovic, V. (2011). Numerical and analytical model-
 689 ing of advective travel times in realistic three-dimensional fracture net-
 690 works. *Water Resources Research*, 47(2). Retrieved 2022-04-05, from
 691 <https://onlinelibrary.wiley.com/doi/abs/10.1029/2010WR009290>
 692 (_eprint: <https://onlinelibrary.wiley.com/doi/pdf/10.1029/2010WR009290>)
 693 doi: 10.1029/2010WR009290
- 694 Frampton, A., Hyman, J. D., & Zou, L. (2019). Advective Transport in
 695 Discrete Fracture Networks With Connected and Disconnected Tex-
 696 tures Representing Internal Aperture Variability. *Water Resources*
 697 *Research*, 55(7), 5487–5501. Retrieved 2022-04-05, from [https://](https://onlinelibrary.wiley.com/doi/abs/10.1029/2018WR024322)
 698 onlinelibrary.wiley.com/doi/abs/10.1029/2018WR024322 (_eprint:
 699 <https://onlinelibrary.wiley.com/doi/pdf/10.1029/2018WR024322>) doi:
 700 10.1029/2018WR024322
- 701 Gallant, J. C., Moore, I. D., Hutchinson, M. F., & Gessler, P. (1994, May). Estimat-
 702 ing fractal dimension of profiles: A comparison of methods. *Mathematical Ge-*
 703 *ology*, 26(4), 455–481. Retrieved 2022-09-01, from [https://doi.org/10.1007/](https://doi.org/10.1007/BF02083489)
 704 [BF02083489](https://doi.org/10.1007/BF02083489) doi: 10.1007/BF02083489
- 705 Glover, P. W. J., Matsuki, K., Hikima, R., & Hayashi, K. (1998a). Fluid
 706 flow in synthetic rough fractures and application to the Hachimantai
 707 geothermal hot dry rock test site. *Journal of Geophysical Research:*
 708 *Solid Earth*, 103(B5), 9621–9635. Retrieved 2022-02-15, from [https://](https://onlinelibrary.wiley.com/doi/abs/10.1029/97JB01613)
 709 onlinelibrary.wiley.com/doi/abs/10.1029/97JB01613 (_eprint:
 710 <https://onlinelibrary.wiley.com/doi/pdf/10.1029/97JB01613>) doi: 10.1029/
 711 97JB01613
- 712 Glover, P. W. J., Matsuki, K., Hikima, R., & Hayashi, K. (1998b). Syn-
 713 thetic rough fractures in rocks. *Journal of Geophysical Research: Solid*
 714 *Earth*, 103(B5), 9609–9620. Retrieved 2022-11-10, from [https://](https://onlinelibrary.wiley.com/doi/abs/10.1029/97JB02836)
 715 onlinelibrary.wiley.com/doi/abs/10.1029/97JB02836 (_eprint:
 716 <https://onlinelibrary.wiley.com/doi/pdf/10.1029/97JB02836>) doi: 10.1029/
 717 97JB02836
- 718 Hakami, E. (1995). *Aperture distribution of rock fractures* (Tech. Rep. Nos. KTH-
 719 AMI-PHD-1003). Royal Inst. of Tech. Retrieved 2020-07-30, from [http://](http://inis.iaea.org/Search/search.aspx?orig_q=RN:27020199)
 720 inis.iaea.org/Search/search.aspx?orig_q=RN:27020199

- 721 Hurst, H. E. (1951, January). Long-Term Storage Capacity of Reservoirs.
 722 *Transactions of the American Society of Civil Engineers*, 116(1), 770–799.
 723 Retrieved 2022-09-01, from [https://ascelibrary.org/doi/10.1061/](https://ascelibrary.org/doi/10.1061/TACEAT.0006518)
 724 TACEAT.0006518 (Publisher: American Society of Civil Engineers) doi:
 725 10.1061/TACEAT.0006518
- 726 Isakov, E., Ogilvie, S. R., Taylor, C. W., & Glover, P. W. J. (2001, September).
 727 Fluid flow through rough fractures in rocks I: high resolution aperture deter-
 728 minations. *Earth and Planetary Science Letters*, 191(3), 267–282. Retrieved
 729 2023-01-03, from [https://www.sciencedirect.com/science/article/pii/](https://www.sciencedirect.com/science/article/pii/S0012821X01004241)
 730 S0012821X01004241 doi: 10.1016/S0012-821X(01)00424-1
- 731 Keller, A. A., Roberts, P. V., & Blunt, M. J. (1999). Effect of fracture
 732 aperture variations on the dispersion of contaminants. *Water Re-*
 733 *sources Research*, 35(1), 55–63. Retrieved 2023-01-03, from [https://](https://onlinelibrary.wiley.com/doi/abs/10.1029/1998WR900041)
 734 onlinelibrary.wiley.com/doi/abs/10.1029/1998WR900041 (_eprint:
 735 <https://onlinelibrary.wiley.com/doi/pdf/10.1029/1998WR900041>) doi:
 736 10.1029/1998WR900041
- 737 Lang, P. S., Paluszny, A., & Zimmerman, R. W. (2014). Permeability ten-
 738 sor of three-dimensional fractured porous rock and a comparison to
 739 trace map predictions. *Journal of Geophysical Research: Solid Earth*,
 740 119(8), 6288–6307. Retrieved 2020-09-12, from [https://agupubs](https://agupubs.onlinelibrary.wiley.com/doi/abs/10.1002/2014JB011027)
 741 [.onlinelibrary.wiley.com/doi/abs/10.1002/2014JB011027](https://agupubs.onlinelibrary.wiley.com/doi/abs/10.1002/2014JB011027) (_eprint:
 742 <https://agupubs.onlinelibrary.wiley.com/doi/pdf/10.1002/2014JB011027>) doi:
 743 10.1002/2014JB011027
- 744 Malinverno, A. (1990). A simple method to estimate the fractal dimen-
 745 sion of a self-affine series. *Geophysical Research Letters*, 17(11),
 746 1953–1956. Retrieved 2021-11-29, from [https://onlinelibrary](https://onlinelibrary.wiley.com/doi/abs/10.1029/GL017i011p01953)
 747 [.wiley.com/doi/abs/10.1029/GL017i011p01953](https://onlinelibrary.wiley.com/doi/abs/10.1029/GL017i011p01953) (_eprint:
 748 <https://onlinelibrary.wiley.com/doi/pdf/10.1029/GL017i011p01953>) doi:
 749 10.1029/GL017i011p01953
- 750 Mandelbrot, B. (1982). *The Fractal Geometry of Nature* (Vol. 1). WH Freeman New
 751 York.
- 752 Marsch, K., & Fernandez-Steege, T. M. (2021, April). Comparative Evaluation
 753 of Statistical and Fractal Approaches for JRC Calculation Based on a Large
 754 Dataset of Natural Rock Traces. *Rock Mechanics and Rock Engineering*, 54(4),
 755 1897–1917. Retrieved 2021-11-24, from [http://link.springer.com/10.1007/](http://link.springer.com/10.1007/s00603-020-02348-0)
 756 s00603-020-02348-0 doi: 10.1007/s00603-020-02348-0
- 757 Nicholl, M. J., Rajaram, H., Glass, R. J., & Detwiler, R. (1999). Sat-
 758 urated flow in a single fracture: evaluation of the Reynolds Equa-
 759 tion in measured aperture fields. *Water Resources Research*,
 760 35(11), 3361–3373. Retrieved 2020-08-31, from [https://agupubs](https://agupubs.onlinelibrary.wiley.com/doi/abs/10.1029/1999WR900241)
 761 [.onlinelibrary.wiley.com/doi/abs/10.1029/1999WR900241](https://agupubs.onlinelibrary.wiley.com/doi/abs/10.1029/1999WR900241) (_eprint:
 762 <https://agupubs.onlinelibrary.wiley.com/doi/pdf/10.1029/1999WR900241>) doi:
 763 10.1029/1999WR900241
- 764 Novakowski, K. S., & Lapcevic, P. A. (1994). Field measurement of
 765 radial solute transport in fractured rock. *Water Resources Re-*
 766 *search*, 30(1), 37–44. Retrieved 2020-08-31, from [https://agupubs](https://agupubs.onlinelibrary.wiley.com/doi/abs/10.1029/93WR02401)
 767 [.onlinelibrary.wiley.com/doi/abs/10.1029/93WR02401](https://agupubs.onlinelibrary.wiley.com/doi/abs/10.1029/93WR02401) (_eprint:
 768 <https://agupubs.onlinelibrary.wiley.com/doi/pdf/10.1029/93WR02401>) doi:
 769 10.1029/93WR02401
- 770 Ogilvie, S. R., Isakov, E., & Glover, P. W. (2006, January). Fluid flow through
 771 rough fractures in rocks. II: A new matching model for rough rock frac-
 772 tures. *Earth and Planetary Science Letters*, 241(3-4), 454–465. Retrieved
 773 2021-10-05, from [https://linkinghub.elsevier.com/retrieve/pii/](https://linkinghub.elsevier.com/retrieve/pii/S0012821X05008174)
 774 S0012821X05008174 doi: 10.1016/j.epsl.2005.11.041
- 775 Ogilvie, S. R., Isakov, E., Taylor, C. W., & Glover, P. W. J. (2003, January).

- 776 Characterization of rough-walled fractures in crystalline rocks. *Geolog-*
 777 *ical Society, London, Special Publications, 214* (1), 125–141. Retrieved
 778 2023-01-03, from [https://www.lyellcollection.org/doi/abs/10.1144/](https://www.lyellcollection.org/doi/abs/10.1144/gsl.sp.2003.214.01.08)
 779 [gsl.sp.2003.214.01.08](https://www.lyellcollection.org/doi/abs/10.1144/gsl.sp.2003.214.01.08) (Publisher: The Geological Society of London) doi:
 780 10.1144/GSL.SP.2003.214.01.08
- 781 Power, W. L., & Tullis, T. E. (1991). Euclidean and fractal models for the
 782 description of rock surface roughness. *Journal of Geophysical Research:*
 783 *Solid Earth, 96*(B1), 415–424. Retrieved 2022-09-01, from [https://](https://onlinelibrary.wiley.com/doi/abs/10.1029/90JB02107)
 784 onlinelibrary.wiley.com/doi/abs/10.1029/90JB02107 (_eprint:
 785 <https://onlinelibrary.wiley.com/doi/pdf/10.1029/90JB02107>) doi: 10.1029/
 786 90JB02107
- 787 Power, W. L., & Tullis, T. E. (1992). The contact between opposing fault surfaces
 788 at Dixie Valley, Nevada, and implications for fault mechanics. *Journal of Geo-*
 789 *physical Research: Solid Earth, 97*(B11), 15425–15435. Retrieved 2022-02-15,
 790 from <https://onlinelibrary.wiley.com/doi/abs/10.1029/92JB01059>
 791 (_eprint: <https://onlinelibrary.wiley.com/doi/pdf/10.1029/92JB01059>) doi:
 792 10.1029/92JB01059
- 793 Renard, F., Voisin, C., Marsan, D., & Schmittbuhl, J. (2006). High res-
 794 olution 3D laser scanner measurements of a strike-slip fault quan-
 795 tify its morphological anisotropy at all scales. *Geophysical Re-*
 796 *search Letters, 33*(4). Retrieved 2021-09-15, from [https://](https://onlinelibrary.wiley.com/doi/abs/10.1029/2005GL025038)
 797 onlinelibrary.wiley.com/doi/abs/10.1029/2005GL025038 (_eprint:
 798 <https://agupubs.onlinelibrary.wiley.com/doi/pdf/10.1029/2005GL025038>) doi:
 799 10.1029/2005GL025038
- 800 Stigsson, M., & Mas Ivars, D. (2019, April). A Novel Conceptual Approach to Ob-
 801 jectively Determine JRC Using Fractal Dimension and Asperity Distribution
 802 of Mapped Fracture Traces. *Rock Mechanics and Rock Engineering, 52*(4),
 803 1041–1054. Retrieved 2021-05-26, from [http://link.springer.com/10.1007/](http://link.springer.com/10.1007/s00603-018-1651-6)
 804 [s00603-018-1651-6](http://link.springer.com/10.1007/s00603-018-1651-6) doi: 10.1007/s00603-018-1651-6
- 805 Stock, B. (2023, September). *Fracture surface data* [dataset]. Retrieved from
 806 <https://doi.org/10.5281/zenodo.8354914> doi: 10.5281/zenodo.8354914
- 807 Stock, B., & Frampton, A. (2022, June). Processing and Conversion of Raw Point-
 808 Cloud Laser Measurements and Auxiliary Data of Rough-Surfaced Fractures
 809 To Generate Corresponding Fracture Aperture Fields. OnePetro. Retrieved
 810 2023-05-16, from [https://onepetro.org/ARMADFNE/proceedings-abstract/](https://onepetro.org/ARMADFNE/proceedings-abstract/DFNE22/A11-DFNE22/515893)
 811 [DFNE22/A11-DFNE22/515893](https://onepetro.org/ARMADFNE/proceedings-abstract/DFNE22/A11-DFNE22/515893) doi: 10.56952/ARMA-DFNE-22-0020
- 812 Tsang, C.-F., & Neretnieks, I. (1998). Flow channeling in heterogeneous frac-
 813 tured rocks. *Reviews of Geophysics, 36*(2), 275–298. Retrieved 2022-08-24,
 814 from <https://onlinelibrary.wiley.com/doi/abs/10.1029/97RG03319>
 815 (_eprint: <https://onlinelibrary.wiley.com/doi/pdf/10.1029/97RG03319>) doi:
 816 10.1029/97RG03319
- 817 Witherspoon, P. A., Wang, J. S. Y., Iwai, K., & Gale, J. E. (1980). Validity of
 818 Cubic Law for fluid flow in a deformable rock fracture. *Water Resources*
 819 *Research, 16*(6), 1016–1024. Retrieved 2020-07-21, from [https://agupubs](https://agupubs.onlinelibrary.wiley.com/doi/abs/10.1029/WR016i006p01016)
 820 [.onlinelibrary.wiley.com/doi/abs/10.1029/WR016i006p01016](https://agupubs.onlinelibrary.wiley.com/doi/abs/10.1029/WR016i006p01016) (_eprint:
 821 <https://agupubs.onlinelibrary.wiley.com/doi/pdf/10.1029/WR016i006p01016>)
 822 doi: 10.1029/WR016i006p01016
- 823 Zimmerman, R. W., & Bodvarsson, G. S. (1996, April). Hydraulic conductivity of
 824 rock fractures. *Transport in Porous Media, 23*(1), 1–30. Retrieved 2019-11-11,
 825 from <https://doi.org/10.1007/BF00145263> doi: 10.1007/BF00145263
- 826 Zou, L., Jing, L., & Cvetkovic, V. (2017, September). Modeling of flow
 827 and mixing in 3D rough-walled rock fracture intersections. *Advances*
 828 *in Water Resources, 107*, 1–9. Retrieved 2021-06-14, from [https://](https://www.sciencedirect.com/science/article/pii/S0309170816305097)
 829 www.sciencedirect.com/science/article/pii/S0309170816305097 doi:
 830 10.1016/j.advwatres.2017.06.003